ANIMAL ROBOTS

BirdBot achieves energy-efficient gait with minimal control using avian-inspired leg clutching

Alexander Badri-Spröwitz[1]*†, Alborz Aghamaleki Sarvestani[1]†, Metin Sitti[2,3,4], Monica A. Daley[5,6]

Designers of legged robots are challenged with creating mechanisms that allow energy-efficient locomotion with robust and minimalistic control. Sources of high energy costs in legged robots include the rapid loading and high forces required to support the robot's mass during stance and the rapid cycling of the leg's state between stance and swing phases. Here, we demonstrate an avian-inspired robot leg design, BirdBot, that challenges the reliance on rapid feedback control for joint coordination and replaces active control with intrinsic, mechanical coupling, reminiscent of a self-engaging and disengaging clutch. A spring tendon network rapidly switches the leg's slack segments into a loadable state at touchdown, distributes load among joints, enables rapid disengagement at toe-off through elastically stored energy, and coordinates swing leg flexion. A bistable joint mediates the spring tendon network's disengagement at the end of stance, powered by stance phase leg angle progression. We show reduced knee-flexing torque to a 10th of what is required for a nonclutching, parallel-elastic leg design with the same kinematics, whereas spring-based compliance extends the leg in stance phase. These mechanisms enable bipedal locomotion with four robot actuators under feedforward control, with high energy efficiency. The robot offers a physical model demonstration of an avian-inspired, multiarticular elastic coupling mechanism that can achieve self-stable, robust, and economic legged locomotion with simple control and no sensory feedback. The proposed design is scalable, allowing the design of large legged robots. BirdBot demonstrates a mechanism for self-engaging and disengaging parallel elastic legs that are contact-triggered by the foot's own lever-arm action.

INTRODUCTION

Agile legged locomotion in robots remains a challenge at the frontiers of science (*1*–*4*). No current bipedal robot can run quickly, untethered, in natural environments over long distances. However, these activities are commonplace for terrestrial animals. Despite the apparent agility of running animals, legged locomotion is complex and requires robust control of leg-substrate interaction forces in the face of terrain variation and sensorimotor noise (*5*–*8*). Innovation is needed to design legged robots that achieve low energy consumption locomotion (*9*) with robust mechanics and simple control. For operational robustness, the system should be able to deal with external perturbations that occur faster than communication delays and actuator response times (*10*). Hence, systems should minimize dependence on communication speed and sensor quality.

In biological systems, the prevailing theory suggests that legged animals coordinate joint actuation through antagonistic pairs of muscles controlled by spinal sensorimotor circuits, functioning as "myotatic units" (Fig. 1B) (*11*–*15*). The myotatic unit concept is mimicked in robotics through the control of joint extension and flexion by separate actuators at each joint. Joint actuation is typically controlled through complex, optimized algorithms that rely on internal robot models and rapid sensory feedback loops (*16*). Phase transitions are controlled through contact and load sensors at the feet or within the leg structure (*17*), or as "proprioceptive" sensing within the actuator's electrical circuits (*18*). With fast sensory feedback and communication, robots can smoothly transition through the gait cycle and react to unforeseen perturbations (*19*, *20*). However, the robustness and agility of legged robots remain limited. Paradoxically, animals vastly outperform current robots despite considerably slower sensing and information transfer rates (*10*, *21*, *22*).

Previous evidence suggests the potential for embodied, intrinsic mechanics and interjoint mechanical coupling in vertebrates' legs

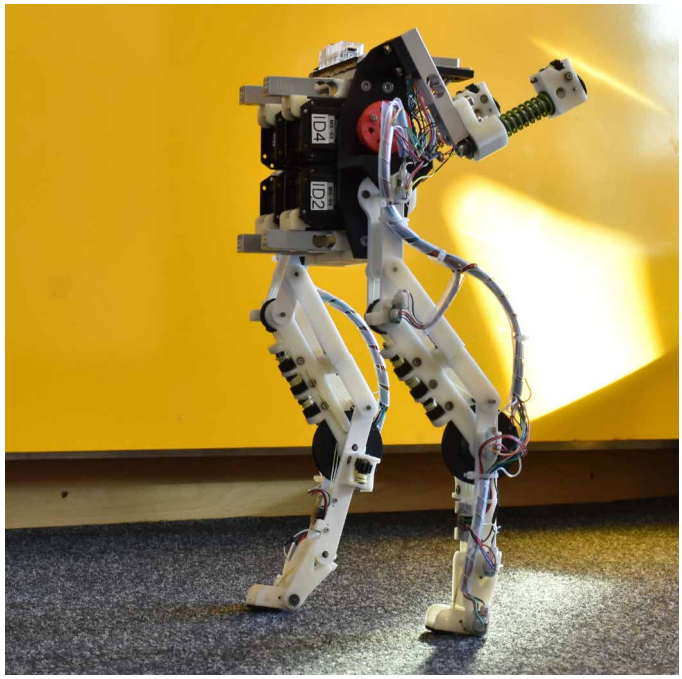

Movie 1. Overview of BirdBot. The robot is inspired by the multijoint, elastic tendon mechanism of the lower leg in large birds.

[1]Dynamic Locomotion Group, Max Planck Institute for Intelligent Systems, Stuttgart, Germany. [2]Physical Intelligence Department, Max Planck Institute for Intelligent Systems, Stuttgart, Germany. [3]Institute for Biomedical Engineering, ETH-Zürich, Zürich, Switzerland. [4]School of Medicine and College of Engineering, Koç University, Istanbul, Turkey. [5]Department of Ecology and Evolutionary Biology, University of California, Irvine, CA, USA. [6]Royal Veterinary College, London, UK.
*Corresponding author. Email: sprowitz@is.mpg.de
†These authors contributed equally to this work.

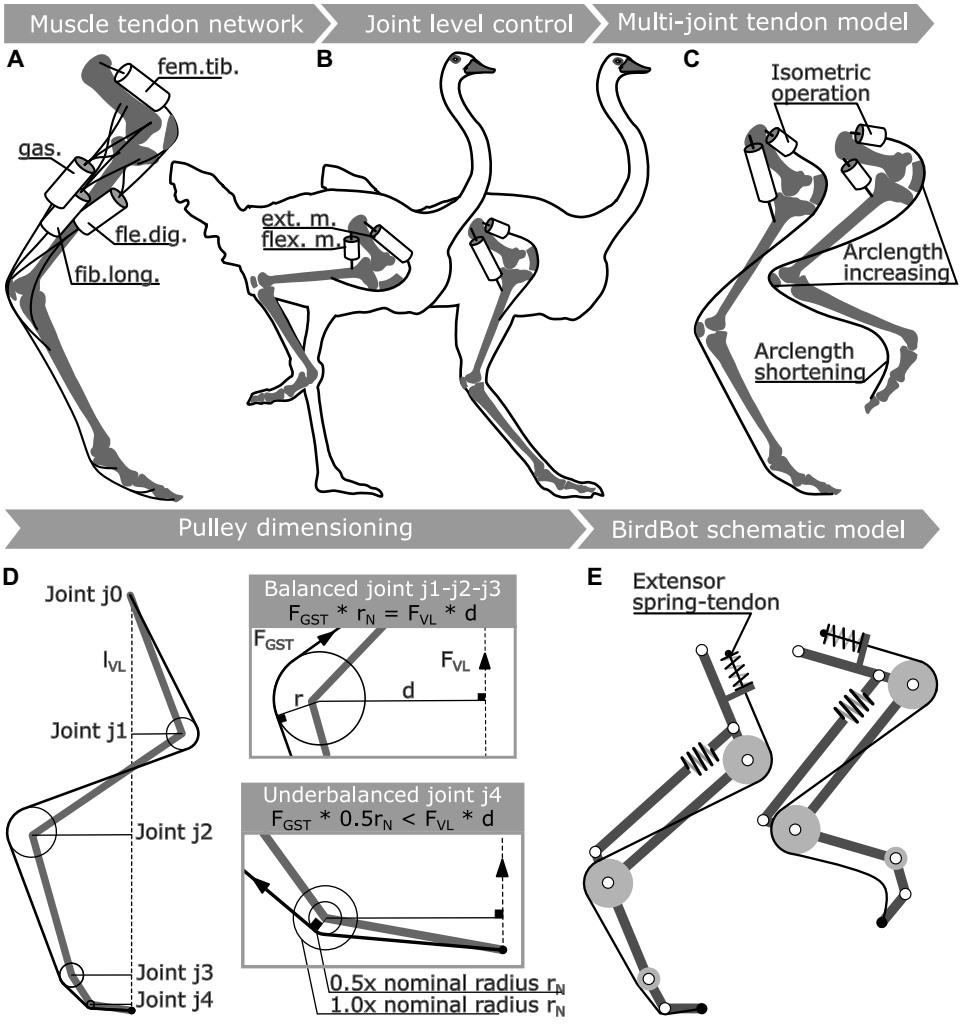

Fig. 1. Biologically inspired design of BirdBot's leg. (**A**) Major muscle-tendon networks that contribute to coordinated stance leg extension and weight support in large ratite birds such as emus and ostriches. Figure inspired from (*61*). (**B**) Classic theory suggests that joints are coordinated by flexor-extensor pairs at each joint, acting as myotatic units. However, in birds, distal joints are actuated by a multiarticular musculotendon network. Figure modified from (*126*). (**C**) Mechanical analysis demonstrates that a solution exists for a single, multiarticular tendon to support stance loads and allow the leg to be fully flexed for swing. The increase in arclength from knee and ankle flexion is balanced by the shortened arclength at the distal distal joints, with tendon slack at the distal joints. The change from stance to swing configuration requires no net change in length, so it is feasible for a muscle acting in series to contract isometrically. (**D**) In BirdBot's leg design, we dimensioned all but the most distal pulleys to balance the external joint moment (F_{VL} d) against internal joint moment (F_{GST} r_N). All joints share an equal global tendon force F_{GST}. The distal pulley radius is 0.5 times of the nominal pulley radius r_N. The underbalanced distal joint results in rapid digital extension into a flat-foot position under load. (**E**) Together, the multiarticular tendon and pulley design create a self-engaging clutch for the stance leg, which provides bodyweight support and distributes force and power among the joints. The foot's lever-action mechanically releases and slacks the multiarticular tendon in swing phase. BirdBot's leg design enables bipedal locomotion with minimalistic feedforward control.

to simplify control (*6*, *23*–*32*). Multiarticular muscle-tendon coupling can facilitate energy transfer between joints and improve efficiency by allowing muscles to work closer to optimal length and velocity (*33*–*36*). Nonetheless, the role of multiarticular mechanisms in the control of animal locomotion remains poorly understood. A challenge for demonstrating the role of embodied, intrinsic mechanics in animal locomotion is that both active neural and intrinsic mechanical control occur simultaneously (*5*, *7*, *37*, *38*). This makes it nearly impossible to disentangle the contributions of each. Robot experiments provide an opportunity to directly demonstrate the function of intrinsic mechanical coupling, using a physical model of the salient musculoskeletal features to test hypotheses about biological function while also inspiring innovations in robot leg design (*2*, *39*).

BirdBot showcases a foot contact-based, self-engaging leg spring clutch mechanism (Movie 1). It is minimally actuated with two actuators per leg—hip joint protraction and retraction and knee flexion actuators—controlled in feedforward mode. BirdBot builds upon established mechanisms and principles including cable-and-pulley–driven actuation, tendons routed over multiple joints ("multiarticular" tendons), clutching of leg forces, parallel and series leg elasticity during stance, and slack leg joints during swing. BirdBot's clutching mechanism engages and disengages robustly with no feedback control. Our design framework demonstrates how intrinsic leg mechanics can enable self-stable and economical gait with consistent phase transitions that are robust to variation under initial conditions.

Many legged animals show coupled joint kinematics, mediated by multiarticular muscle-tendon units, suggesting that such mechanisms are an essential feature of leg design and control in terrestrial animals (*31*, *36*, *40*, *41*). Passive mechanical coupling of joints through multiarticular muscle-tendons without active central nervous system control has been directly observed in frogs, horses, and ratites (*23*, *24*, *31*, *40*). Bioinspired robots and exoskeletons have demonstrated functional benefits of coupled joints by creating analogous structures using spring-loaded four-bar, pantograph, and multiarticular cable mechanisms (*42*–*47*). Multiarticular mechanisms enable lightweight leg designs, with the heavy actuators mounted proximally. For example, the Spring Flamingo robot has series elastic actuators in its trunk, with leg joints actuated by long tendons routed over pulleys (*48*). Such mechanically elastic legs also mimic the spring-like function observed in animal gaits (*45*, *48*–*51*). The MIT Cheetah robot's leg mounts a stiff belt as an Achilles tendon spanning multiple joints in a tensegrity structure, which maximizes the leg's strength to weight ratio (*52*). Kurokawa *et al.* (*53*) designed a biarticular mechanism that couples ankle and toe movement, enabling transfer of energy between leg joints for jumping. Mechanically coupled actuators can reduce overall work

and force demands and thereby improve energy efficiency in robots, exoskeletons, and prosthetic devices (*54*, *55*).

Our approach also draws inspiration from research in passive mechanical walking robots that demonstrate locomotion principles with either no actuation or minimal actuation under open loop control. Purely mechanical walkers convert potential energy from a slope into center of mass and swing leg motion (*56*). Related minimally actuated walkers achieve the lowest cost of transport (COT) among legged walking machines (*57*). Mechanical walkers and their models illustrate principles for economic walking by identifying sources of energy loss and fluctuation, including inelastic collisions between the foot and the ground, redirecting the center of mass velocity at foot impact, achieving ground clearance during forward leg swing, carrying the robot's weight during stance, and joint friction (*56*–*60*). Although exceptionally energy efficient, passive mechanical walking robots remain limited to flat, smooth terrain, and their stability is sensitive to initial conditions and small perturbations. They have low foot-ground clearance, and even small perturbations such as bouncing joint locks can be destabilizing (*59*).

In this study, we test the hypothesis that an avian-inspired linkage mechanism can replace most of the neural circuitry required to control leg trajectory and transitions between stance and swing phases (Fig. 1). In an iterative design process, we developed a multijoint linkage mechanism fully integrated into a bipedal robot's legs that achieves consistent interjoint coordination and rapid, automatic phase transitions between stance and swing. The leg design was inspired by the muscle-tendon units of large ratite birds, such as the emu (*Dromaius novaehollandiae*) and ostriches (*Struthio* species), but the abstracted structural elements are common among ground-moving birds (*6*, *23*, *24*, *30*, *61*–*67*). A multiarticular spring network guides the leg trajectory and provides a rapid transition between stance and swing using a mechanism reminiscent of a self-engaging and disengaging clutch. We demonstrated the leg mechanism on a treadmill, held by a four-bar guide that allows free vertical and fore-aft horizontal translations but limits sideways translation, pitch, yaw, and roll. We documented the design process, mechanical features, and locomotor dynamics of BirdBot, which embodies mechanics and control elements conceived according to anatomical and functional features of avian locomotion (*6*, *24*, *67*).

RESULTS

We used a robot leg design as a physical model to test the hypothesis that a rigorously designed multiarticular spring tendon network can fully support locomotor loads during stance, coordinate the transfer of mechanical load among the joints, and enable automatic stance/swing phase transitions (Fig. 1). The distal segment's (foot) lever action and a global spring tendon (GST) automatically switch the leg's joints into a loadable state during touchdown and mechanically distribute torques among joints during stance (Fig. 1D). A dedicated tendon disengagement mechanism supports stance-to-swing transition during toe-off by actuating a snap-through (bistable) joint using elastically stored energy. The GST and the compliant four-bar linkage couple leg joints into coordinated leg flexion during swing and rapidly create foot ground clearance for swift leg protraction. BirdBot was designed as a proof-of-concept planarized bipedal robot, with high-geared (200:1 ratio), brushed-motor actuators that enable moderate frequencies and speeds [Froude number Fr = $v^2/(gl) = (0.75\ \mathrm{m/s})^2/(9.81\ \mathrm{m/s^2} \cdot 0.29\ \mathrm{m}) = 0.20$], but not fast running.

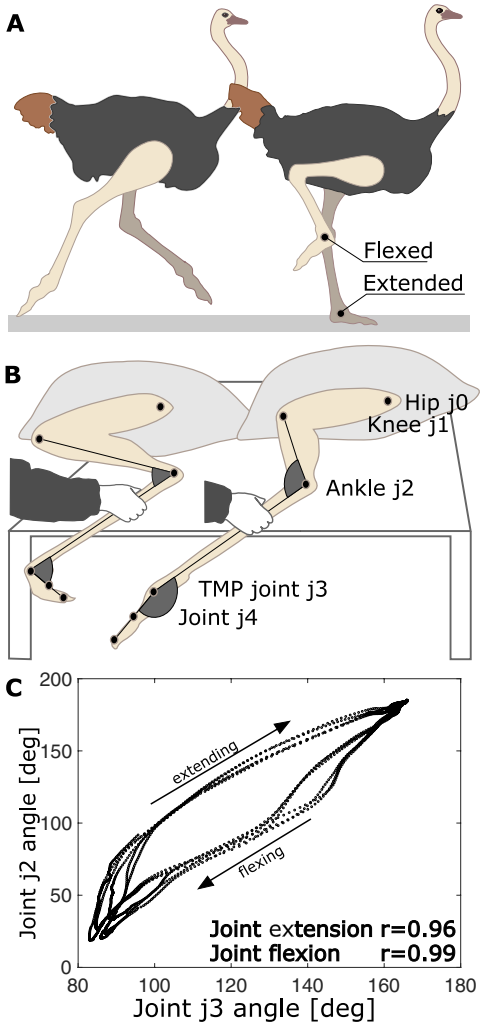

Fig. 2. Mechanical coupling of distal joints in the ratite leg. (**A**) In the running ratite birds, the digits are digital-flexed in swing and digital-extended upon knee extension in preparation for stance. (**B**) The distal avian hindlimb exhibits passive mechanical joint coupling, which can be determined by manually flexing and extending the ankle joint, j2, and measuring coupled motions at the TMP joint, j3. (**C**) Strong coupling exists between the two joints in both flexion and extension, demonstrated by correlation coefficients of $r = 0.99$ and $r = 0.96$, respectively.

The bioinspired features, design process, and resulting gait mechanics are detailed below.

We measured the joint angular coupling in an emu cadaver leg by manually moving the tibiotarsus in an unloaded leg while observing the coupled flexion and extension of the ankle and tarsometatarso-phalangeal (TMP) joints (Fig. 2, A to C). Upon manually flexing and extending the ankle joint j2, we measured coupled motions at the TMP joint j3. Strong coupled motion between the ankle and TMP is evidence based on an observed correlation coefficient of 0.96 for extension and 0.99 for flexion (Fig. 2C). In our measurements, the mechanical coupling arose only from passive tissue elasticity because the central nervous system was inactive. Sources of passive tissue connectivity in the avian limb include the proximal origins of major ankle extensors and digital flexors from the patellar tendofascial sheet at the knee (*68*), and

ligament connectivity between distal joints including the intertarsal joint (Fig. 1A) (*23*, *24*). In particular, Schaller *et al.* (*24*) observed an ankle-locking mechanism based on ligament interactions in ostrich legs, although it remains unclear whether these passive structures alone can fully support body weight in these animals.

To enable a rigorous approach for designing a ratite-inspired tendon network, we initially "linearized" many of the biologically relevant structures. That is, we assumed constant pulley radii and simple hinge joints (Fig. 1, D and E), in place of nonlinear curved sesamoid surfaces and bone surface interactions that lead to a complex, translating center of rotation. Nonetheless, the robot tendon network retains the essential connectivity features of the avian limb. The spring tendon network is designed to establish coupled joint kinematics in swing phase, to flex all joints to provide ground clearance, to engage the global leg spring upon loading into stance phase, to support body weight and distribute torque and power among joints during stance, and to disengage at the end of stance and rapidly transition the leg into the swing phase. The joint coupling during stance distributes the load among the individual joints, without the danger of catastrophic collapse at any single joint, and supports compliant leg compression under load for elastic energy cycling (*49*).

To achieve these mechanical features, we first introduced a single multiarticular spring tendon structure connecting all leg joints (Fig. 1C). We designed a z-like leg structure (Fig. 1, D and E) commonly observed in vertebrates (*69*–*71*). We further assumed a planar configuration, without off-plane influence. Pulley radii r_{jx} of joint j_x were calculated to establish an equal effective mechanical advantage (EMA) (*72*) for all joints sharing the same multiarticular spring tendon ("GST"), with a force magnitude of $\|\vec{F}_{\mathrm{GST}}\|$

$$\|\vec{F}_{\mathrm{VL}}\| \cdot d_{jx} = \|\vec{F}_{\mathrm{GST}}\| \cdot r_{jx} \quad (1)$$

$$r_{jx} = \frac{\|\vec{F}_{\mathrm{VL}}\| \cdot d_{jx}}{\|\vec{F}_{\mathrm{GST}}\|} \quad (2)$$

where $\vec{F}_{\mathrm{VL}}$ is the force along the virtual leg direction l_{VL} (Fig. 1D) and d_{jx} is the shortest distance between joint j_x and the virtual leg l_{VL}. Equation 1 balances joints j1 and j2 equally. For the shown, EMA-balanced configuration in Fig. 1 (D and E) and a given a virtual leg length change, these joint's angles change equally. Each joint's torque balance depends on its pulley's radius and the joint's perpendicular distance to the virtual axis.

Next, we introduced an imbalance between the torque loading of the distal joint j_{distal} (external) and its extension torque (internal). The imbalance serves to securely and compliantly "lock" the leg structure under external load $\|\vec{F}_{\mathrm{VL}}\| > 0$. The imbalance was achieved by underdimensioning the most distal joint's pulley radius relative to its nominal (balanced) value. In place of an EMA-balanced pulley (Eq. 1) with nominal radius (r_{N}), an "underbalanced" pulley with half the EMA-balancing radius was mounted

$$r_{\mathrm{und}} = \frac{r_{\mathrm{N}}}{2} \quad (3)$$

$$\|\vec{F}_{\mathrm{VL}}\| \cdot d_{j,\mathrm{distal}} > \|\vec{F}_{\mathrm{GST}}\| \cdot r_{\mathrm{und}} \quad (4)$$

The underbalanced joint deflected faster compared with the balanced joints. Consequently, when the leg was loaded, the distal joint rapidly collapsed until the most distal segment touched the ground to establish a flat, foot-style contact (movie S7).

With the selected global spring's stiffness, the leg deflected by 10% under three body weights, approximate to that observed in legged animals (*73*–*75*). The resulting leg structure was balanced for static load but would destabilize when transitioned between leg postures or when torques were applied. Therefore, we further stabilized the leg by embedding a spring-loaded pantograph mechanism into the z-shaped leg structure (Figs. 1E and 3A), which also provides compliance in leg angle direction, benefiting energy economy (*76*).

The GST coordinates the motion of all four leg joints during stance phase and rapid transitions to a slack, flexed position in swing (Figs. 3 and 4 and movie S7). When unloaded, the distal joint is released from its clutched, digital-extended position (Fig. 5). The GST becomes slack and detached from the distal pulley, and all leg joints become loose. A central pattern generator (CPG) swing controller (Eq. 9 and fig. S1) commands the knee actuator to flex the knee joint j1, leading to coordinated flexion of all four joints, coupled by the multiarticular and the compliant pantograph. Simultaneously, distal joints j3 and j4 rapidly rotate from their digital-extended position during stance to a pronounced digital flexion in swing, akin to the tarsometatarsus stance-to-swing phase kinematics in running birds (*62*, *63*).

Thus, active knee flexion causes all four joints to rapidly flex toward mid-swing, shortening the leg length for maximum ground clearance (Fig. 4C). The shortened swing leg also reduces the hip torque required to accelerate the leg forward during protraction.

The amount of leg flexion depends on the length of the GST released by the joint j4 digital flexion. Suppose that the multiarticular tendon is wrapped around the pulley of joint j4 (Fig. 4B). In that case, joint j3-j4 digital flexion creates insufficient tendon slack to substantially shorten the leg. The distal tendons of ratite birds such as emus and ostriches are routed in sheaths (*77*) that permit substantial off-joint motion during digital flexion, which we also observed in cadaver dissection (Fig. 4A). We mimic the bird's sheath morphology with a tendon catch (Fig. 4, C and D, and fig. S7) for the otherwise loosely mounted multiarticular tendon. The tendon catch allows for substantial tendon slack during digital flexion and guides the tendon back onto its pulley after digital flexion.

An ideal swing-to-stance transition involves a rapid switch from a slack swing leg to an engaged, load-carrying stance leg that supports body weight and cycles elastic energy. In the late swing phase, the leg length actuator stops flexing the knee joint j1, which effectively lengthens the leg as a result of gravity and the leg's angular momentum. Two distal, biarticular tendons (digit-1 extensor and digit-2 extensor; Fig. 3B) couple the ankle j2 extension to the rotation of the distal joints j3 and j4, into their digital-extended position (Fig. 6A). At the leg's most forward position and while still in air, all leg joints are extended (Fig. 6A, still frame $t = 0.08$ s). Next, the hip actuator pulls the leg backward, into touchdown. As soon as the foot contacts the ground, the GST propagates back the joint j4 lever action to all leg joints. The leg is again locked as a springy strut and ready to carry high mechanical loads throughout stance phase.

An ideal stance-to-swing transition involves a rapid switch from a load-carrying leg to a configuration with all joints slack, allowing rapid leg shortening with low resistance to create ground clearance. In practice, the GST clutching mechanism disengages under the following conditions. The global spring reaches its slack length, which occurs when the leg reaches the disengagement angle (Fig. 5A), and the foot rotates from a digital-extended position to a digital-flexed position to release the GST. Alternatively, disengagement can be

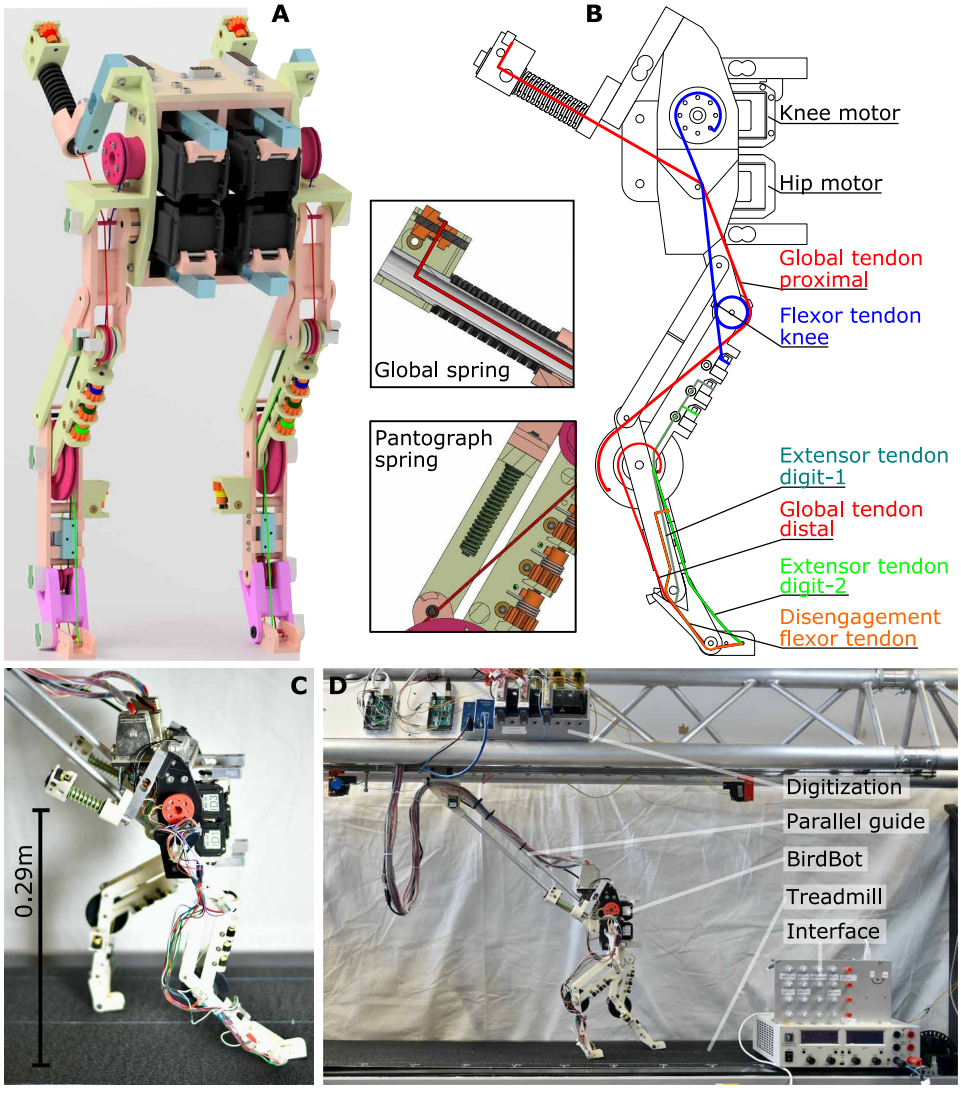

Fig. 3. BirdBot leg design and spring tendon network. (**A**) Computer-aided design drawing of BirdBot. The pantograph spring (spring-12p) is mounted as one-directional elasticity, and the global spring tensions the global multiarticular tendon. Tendon lengths are individually adjusted. (**B**) The GST not only functionally acts across four joints (j1 to j4) but is also guided over hip joint j0. The GST is implemented as two tendons, proximal and distal, connected in the ankle j2 pulley, with different pulley radii. The knee flexor tendon (blue) connects the knee flexion actuator with the tibiotarsus segment, to elevate and shorten the leg during swing. The digit extensors (dark and light green for digit-1 and digit-2) are coupled to ankle j2 action—extension of the ankle pulls both digits into a digital-extended position. The DFT (orange) spans joints j3 and j4 and is actuated by the stance rotation of joint j4 to apply a buckling force at the bistable joint j3 at toe-off to disengage the GST. (**C**) Photo of the BirdBot prototype in side-view, overlaid scale bar. BirdBot's hip height is 0.29 m. (**D**) Experimental setup: treadmill and robot sensor acquisition system. We set gait control parameters through a physical control interface. BirdBot was guided by a four-bar mechanism to constrain pitching, while allowing free fore-aft and vertical translations.

forced through actuation of the distal joint j3 (fig. S11B). At fast speeds, the feedforward actuation patterns cycle the leg length through clutch engagement, mid-stance, and take-off lengths, with the leg lifting off the ground through the robot's momentum. However, at lower speeds, the momentum is insufficient to drive foot lift-off. Consequently, with a digital-extended foot coupled to the global spring through the GST, the foot remains in contact with the GST clutching mechanism engaged. Rotating the foot into a vertical orientation with $\alpha_{j3} > 180°$ angle will reliably disengage the clutch and allow shortening of the slacked leg (fig. S12A). To enable end-stance disengagement with minimal leg work, our aim was to avoid raising the foot to disengage the leg spring. Instead, we added a joint j3 with a disengagement mechanism mediated by a distally mounted, biarticular tendon ["disengagement flexor tendon" (DFT); Fig. 5C and fig. S12B]. The tendon-based disengagement mechanism reduces the work and power required for leg disengagement and works as follows. During stance phase, a joint j3 hard stop only allows joint angles above 160° close to its snap-through angle (Fig. 5C). A biarticular DFT wraps around the joints j3 and j4 (Fig. 5C, DFT, orange tendon). The joint j4 loads the DFT increasingly during stance phase with its joint flexing action. In late stance, the DFT's force pushes the joint j3 over its snap-through angle of 180°. Collapsing joint j3 also slacks the in-parallel GST, which then rapidly slacks all remaining joints into the swing leg configuration (Figs. 4C and 6F and fig. S1).

Both actuators are feedforward controlled by a CPG with two outputs that are interpreted as commanded hip angle and knee angle over time (Eqs. 13 to 16). The hip actuator directly actuates both directions, leg protraction and retraction, whereas the knee actuator transmits flexion torques but no extension torque (fig. S1). The hip output is a sine-like pattern with amplitude A^h oscillating around the femur angle offset O^h. A commanded duty factor adjusts the ratio of swing and stance duration; a duty factor of 0.6 commands a stance phase of 60% of total cycle time. We observe emergent gait patterns with the robot foot already in the air when the femur angle switches from protraction to retraction (end of the commanded swing phase). Consequently, just before touchdown, the hip actuator retracts the leg briefly in air. Similar end-swing characteristics have been shown in underactuated robots with strong natural dynamics (*45*). BirdBot's observed duty factor is 0.49 at a stride frequency of 1.5 Hz (Fig. 6B). In stance, the hip actuator continues to retract the stance leg, propelling the robot forward. As the hip actuator reaches its most posterior angle, leg spring disengagement occurs. The knee actuator starts flexing the knee at the time of leg spring disengagement and, upon disengagement, rapidly flexes the entire leg into the raised swing-leg configuration. The knee actuator starts to release the knee joint

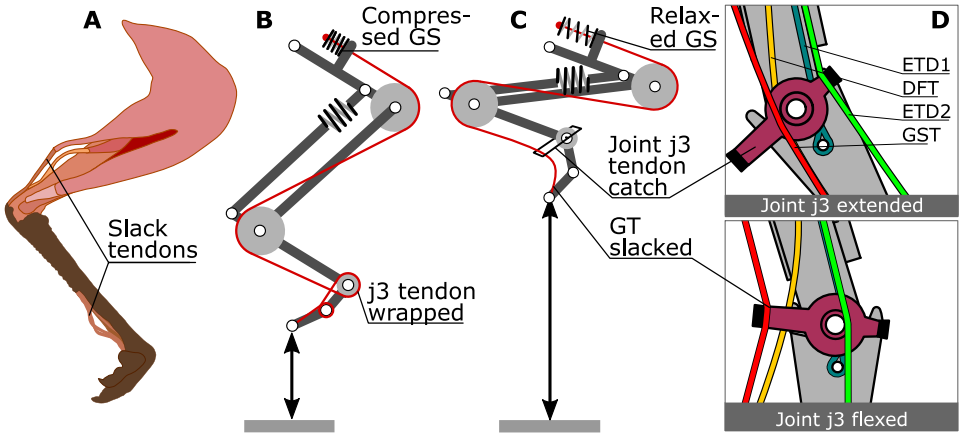

Fig. 4. Enabling tendon slack for low-resistance flexion in swing. (**A**) The distal tendons in the emu and ostrich ratites move loosely within their sheaths at the TMP joint during digital flexion (*77*). (**B**) At the transition from stance to swing, j3 and j4 undergo large digital flexion, which releases the global tendon (GT) length needed to flex the ankle j2 and knee j1. The global tendon can be guided by direct tendon wrapping as shown. However, tight wrapping only releases tendon proportionally to digital flexion angles. Further leg flexion will then load the global spring (GS), which we want to avoid. (**C**) We mimic biological tendon slacking in the robot leg with a detachment and realignment "tendon catch" mechanism at joint j3. This allows full leg flexion without loading the global spring, to achieve low resistance knee flexion without feedback control. (**D**) Mechanism detail: In swing (joint j3 flexed), the global tendon detaches from the j3 pulley. The detachment creates enough tendon slack for full leg shortening.

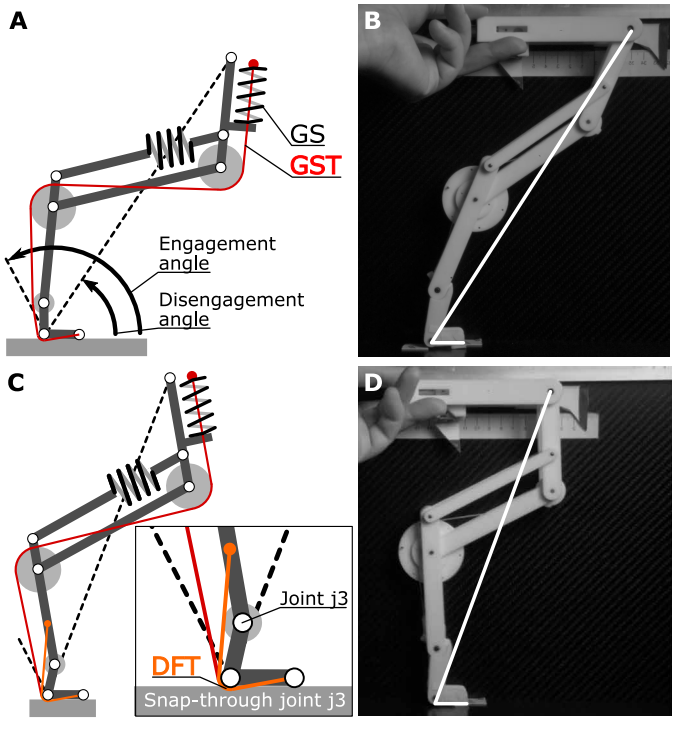

Fig. 5. End stance disengagement. We experimentally measured the disengagement angles with and without the DFT, by manually pushing the hip along a horizontal guide at near-constant speed. (**A**) Without the DFT, leg kinematics unloaded the GST at a virtual leg angle of 59.0° ± 0.3° ("disengagement angle"). (**B**) Snapshot of disengaged leg, like in (A). (**C**) With the DFT, the joint j3 snapped through and unloaded the GST already at a 69.0° ± 1.2° angle, showing a 10° difference caused by the DFT. (**D**) Snapshot of disengaged leg, like in (C). The global spring in the hardware leg is mounted above the hip joint, the modified golden spring schematics in (A) and (C) are shown for simplification.

around mid-swing, and the leg reextends toward the ground. Full leg length is reached at the end of the commanded swing phase, with the leg still in the air and the digital joints extended.

At a 1.5-Hz stride frequency, BirdBot reaches a speed of 0.75 m/s (Froude number Fr = 0.20). In stance phase, a peak retraction torque (leg angle direction) of −1.70 ± 0.05 N·m [confidence interval (CI)] occurred just before midstance (Fig. 6C). During swing phase, the leg angle torque fluctuated between 0.5 N·m at in-air protraction and −0.5 N·m at in-air leg retraction about one-third of the applied leg angle torque during stance (table S5). The torque flexing the knee joint during swing phase reached a maximum of 0.31 ± 0.03 N·m (CI; Fig. 6E, solid line), caused by dynamics of lifting the slack lower leg. This peak torque is comparable in magnitude to the knee-flexing torque required during standing (0.09 N·m statically applied torque; fig. S4 and table S5). In Fig. 6E, we also compare the knee flexing torque of BirdBot with that of a modeled robot with the same morphology but a permanently engaged (nonclutching) knee spring, similar to (*45*). With the additional torque required by the constantly engaged, in-parallel knee spring, the actuator would require 3.7 N·m of torque, or more than 10 times the measured torque of BirdBot's knee, assuming the same knee joint j1 kinematics (Fig. 6G, dashed line, and table S5).

In Fig. 6B, we observe signs of power amplification in the distal tendon work profile, indicated by an asymmetric rate of elastic energy storage and release (*78*). Specifically, the biarticular DFT stored 0.037 ± 0.001 J (CI) elastic energy in the first 82% of the stance phase and released it in the remaining 18% of stance phase, corresponding to an asymmetry ratio of 4.6:1. In comparison, the multiarticular GST stored and released 0.34 ± 0.02 J (CI), on average, about nine times the DFT energy, with relatively symmetric timing around the peak (Fig. 6D and table S3). BirdBot's combined actuators drew in average 15.7 ± 0.4 W and 16.8 ± 0.4 W of electrical net power at 1.0- and 1.5-Hz locomotion, respectively (table S4). The instantaneous electrical power consumption of the hip actuator shows one distinct peak at stance-phase leg retraction (Fig. 7B). The power consumption of the knee actuator peaked twice, following the step-like knee flexion and extension CPG signal (Fig. 7A and fig. S1, A_K). According to Eq. 7, the COT of a natural runner with BirdBot's weight is 1.45 (table S1), and the robot's power consumption at a speed of v = 0.75 m/s corresponds to a net COT of 1.32. It is notoriously hard to compare COT among robots—numerous factors can influence COT including use of mechanical guides (planar four-bar mechanism, rotating boom), varied walking substrate (laboratory surface, treadmill, and outside terrain), power supply (onboard and tethered), control (on-board and remove), motor type (brushes and brushless), gearing, and robot size. BirdBot is guided in-plane by a four-bar while walking on a treadmill, with a pitch-locked trunk, actuated by brushed and high-geared motors, and powered and controller by tether. A freely

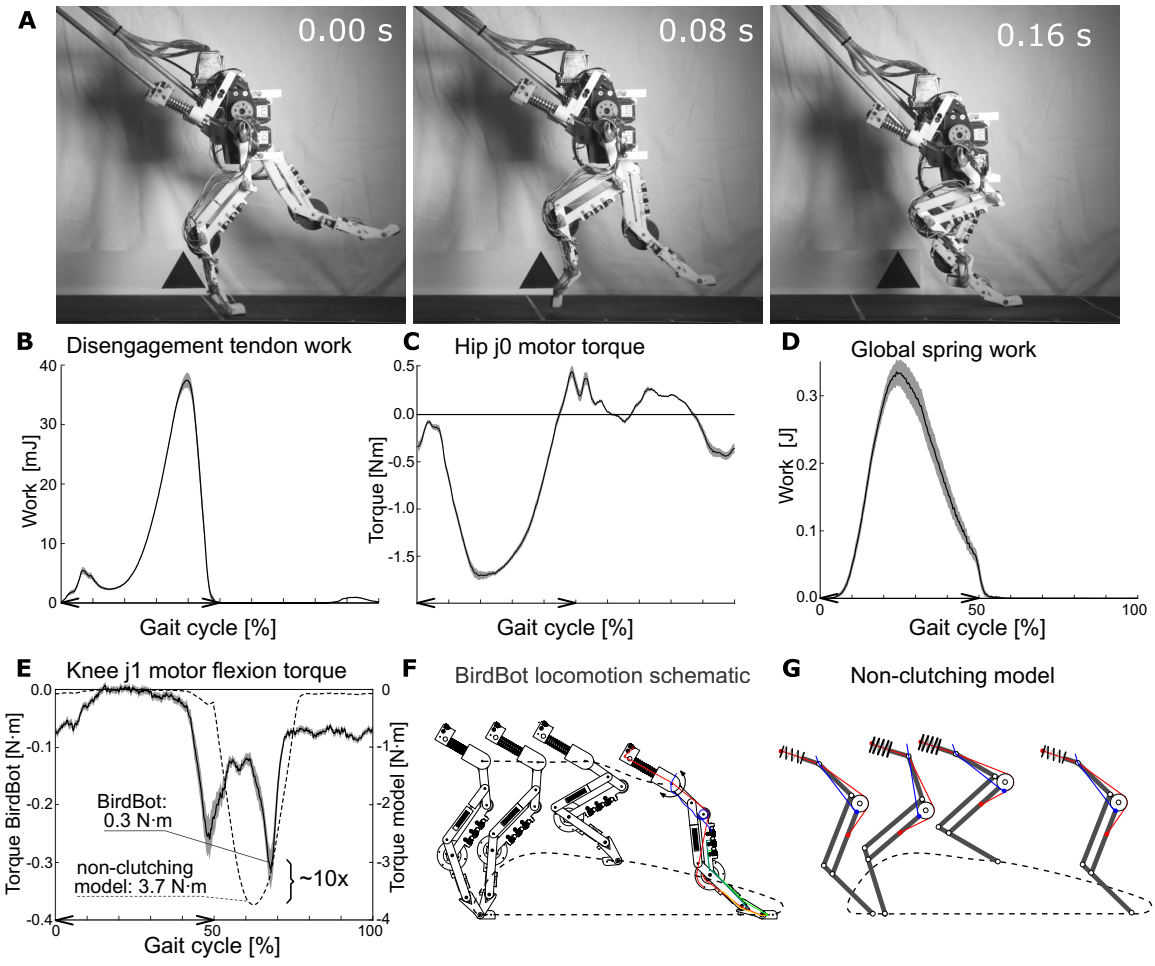

Fig. 6. BirdBot running at a stride frequency of 1.5 Hz, with a speed of 0.75 m/s (Froude number of 0.20). Data are averaged from 70 strides, with a 95% CI shown as a shaded area. The stance period is indicated by "< >" on the *x* axes. (**A**) Side-view video still frames of BirdBot running on the treadmill, with a four-bar guide to restrict rotation. (**B**) The cumulative work applied at the DFT. The tendon stores and releases 0.037 ± 0.001 J (CI) per cycle. The loading and unloading times are asymmetric, indicating power amplification. (**C**) Hip actuator for joint j0 with a peak torque of −1.71 ± 0.05 N·m (CI) during leg retraction at mid-stance. (**D**) The cumulative work applied at the GST, stored and released by the spring as elastic energy. The GST stores on average 0.34 ± 0.02 J (CI) per deflection in this gait. (**E**) The knee flexing actuator applies a peak torque of 0.31 ± 0.03 N·m (CI) at mid-swing to lift the lower leg and create foot-ground clearance (solid line). We modeled a nonclutching, parallel leg spring [dashed line, model shown in (G)] and assumed the same knee joint kinematics as BirdBot. The nonclutched knee actuator model would require 3.7 N·m, which is more than 10 times higher torque than in BirdBot. (**F**) Schematic of BirdBot's leg and foot trajectory over a gait cycle. (**G**) Schematic of the leg and foot trajectory of the nonclutching model.

walking BirdBot would likely consume more power. Nonetheless, BirdBot shows economical locomotion, particularly in comparison with the similarly actuated, freely running robot Cheetah-cub (*45*). To allow indirect comparison between robots, we defined a relative COT in Eq. 8 as the ratio between the robot's COT and that of a natural runner of equal weight, resulting in a relative net COT of 91% for BirdBot.

DISCUSSION

Animals vastly outperform current legged robots, achieving agile movement in natural terrain with robust balance and low metabolic COT, compared with legged robots (*6*, *26*, *79*–*85*). We used an iterative design process and a physical robot to test the hypothesis that a bird-inspired multiarticular linkage mechanism can replace most of the neural circuitry required for joint coordination and stance-swing transition control. The multiarticular spring tendon in the five-segment leg creates a whole-leg clutch, which transitions upon loading into a high stiffness configuration for stance and transitions upon unloading to a slack configuration for swing. The leg design achieves consistent interjoint coordination of a complex leg trajectory, compliant bodyweight support with elastic energy cycling, and rapid, automatic control of swing/stance transitions. The rapid transition to swing is achieved by action of the spring tendon network on a bistable joint, which disengages the stance leg spring. These mechanisms enable bipedal gait with just four actuators under simple, model-free feedforward control. In addition to providing robust mechanics with simple control, the leg design achieves economical COT by reducing knee-flexing torque to $^{1}/_{10}$ of that of nonclutching leg designs similar to Cheetah-cub (*45*).

Research on running ground birds suggested that their remarkable agility and robustness benefit from intrinsic mechanical control (*6*, *26*, *27*, *83*, *86*). BirdBot's leg clutch relies on a digitigrade posture, in which the toe becomes flat against the ground. To freely shorten its leg in swing, the distal segment rotates from a digital-extended

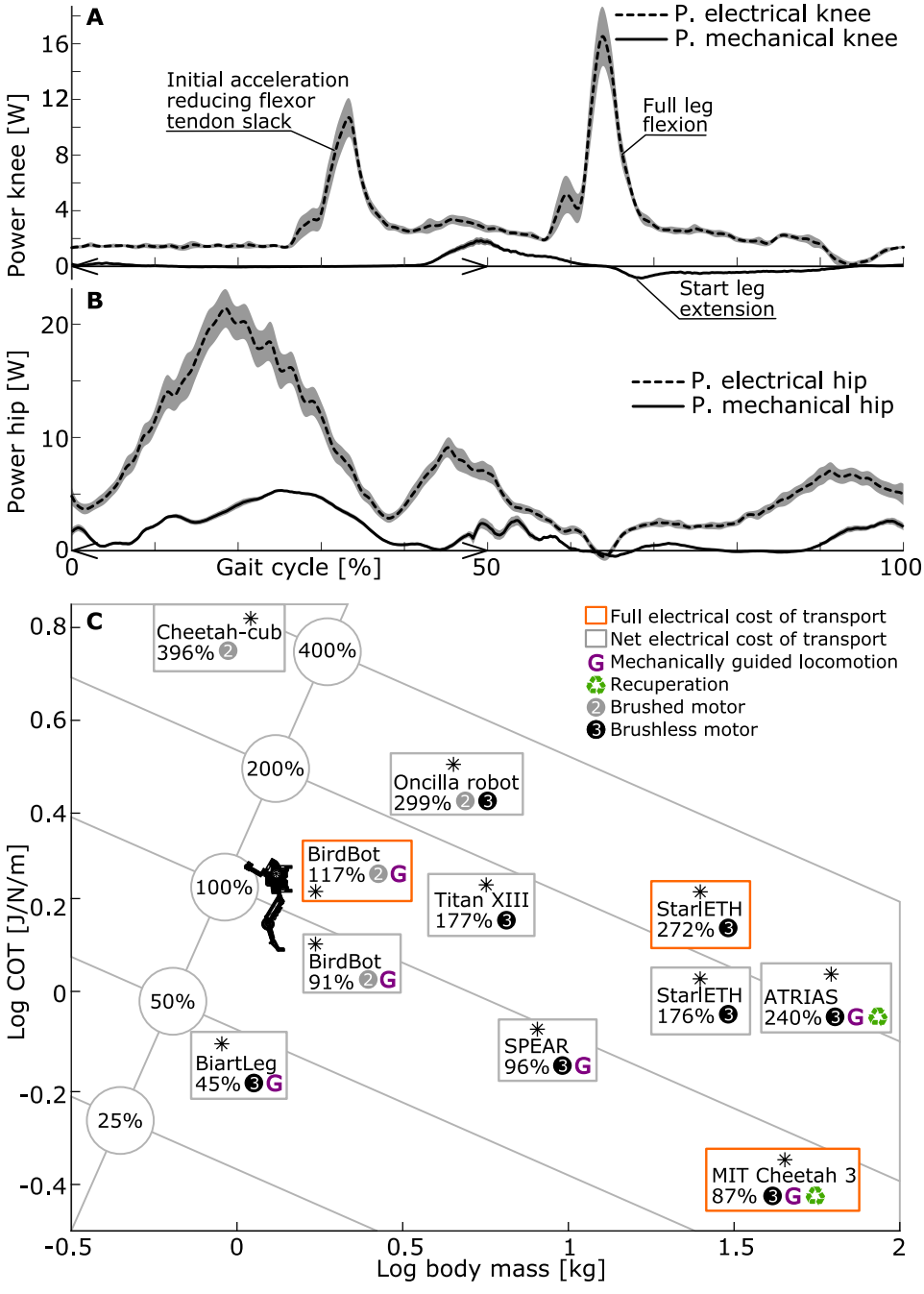

Fig. 7. Robot energetic performance and comparative COT. (**A**) Knee mechanical power (solid line) and instantaneous electrical power of the knee flexing actuator (dashed line). The two electrical power peaks indicate an initial acceleration to reduce tendon slack at the end of stance, and a second burst to fully lift the lower leg in swing. "< >" indicates the observed stance period. (**B**) Hip mechanical power (solid line) and actuator electrical power (dashed line). The highest power consumption occurs during leg retraction in the stance phase. In comparison, swing leg protraction requires considerably less power. (**C**) The electrical COT of selected legged robots, plotted relative to body mass, on a logarithmic scale. As a general reference, the 100% COT line indicates the metabolic cost of animal runners, according to (*120*). Brushless motor–actuated robots that recuperate negative power are indicated with a green recycle symbol. Hopping robots, such as BiartLeg, require no leg shortening for ground clearance in the swing phase, reducing their COT. BirdBot's net COT is slightly below that of a running animal with a similar body mass (1.73 kg). This places BirdBot's net COT in the range of the hopping SPEAR robot and MIT Cheetah 3.

to a digital-flexed posture, which slacks the stance spring. Our analysis suggests a suite of structural features required for the mechanism: elevated, digitigrade posture with a long tarsometatarsus segment, a multiarticular network of ligaments and tendons from femur to toe (Fig. 1C), sesamoid bones creating the appropriate cam dimensions, sheaths to guide slack tendons, and a bistable configuration in the distal joint.

This analysis helps to identify where similar function is likely to be found among diverse animals. Although BirdBot's leg design is inspired by large ratite birds such as emus and ostriches, the structural elements are present to varying degrees among many birds (*6*, *23*, *24*, *30*, *61*–*67*, *87*–*89*). BirdBot is an abstracted and simplified model: Complex bone surface interactions are approximated as hinge joints, and sesamoid structures are approximated as constant radius cams. The model integrates several features: cam radii, distance from the joint center to the virtual leg, segment lengths, and ratios of leg segments. Equations 1 and 3 assume a loading of the virtual leg and establish the required joint moments based on the assumption that all leg joints are mechanically coupled and balanced, resulting in a similar joint velocity for all but the distal joint, which is underdimensioned. Joint coupling propagates loading from proximal and distal and, likewise, distal to proximal. Equations 1 and 4 are indifferent to leg postures (erect or crouched), suggesting that small birds with crouched postures could have a leg clutch. The cam of the distal joint must be underdimensioned, resulting in larger distal joint deflections compared with the knee and ankle. Rapid deflection of the distal joint upon loading creates a flat "foot" contact with the ground and engages the stance leg spring. Disengagement of the stance leg spring is triggered by loading a distal, biarticular tendon, leading to a sudden digital flexion at toe-off. The distal tendon sheath allows tendon detachment and slacking in the swing phase, enabling shortening of the swing leg with low resistance.

Across bird species, the degree to which the leg clutch exists as a passive mechanism likely varies. Ostrich legs have high capacity to

support weight and recycle elastic energy in distal tendons (*65*, *67*) and exhibit the distal structures required for the bistable mechanism (*23*, *24*). Running ostriches also have distal joint kinematics consistent with the leg clutch (*88*). In large ratites, the elastic tissues in the distal leg might passively support body weight, but, in most species, engagement of the leg clutch likely requires active muscle contraction.

The BirdBot model challenges the idea of joint myotatic control, in which antagonistic pairs of flexor and extensor muscles control individual joints (*11*–*13*, *90*). A more modern perspective suggests that muscle synergies control functional modules for whole-leg tasks, such as leg stiffness, bodyweight support, propulsion, leg angular cycling, and balance correction (*8*). Control via functional modules is consistent with observed muscle activation patterns in guineafowl, a terrestrial bird with size similar to BirdBot (*91*, *92*). Coactivation of functional modules could actively engage a leg clutch in species where the mechanism is not passive. In terrestrial birds, for example, isometric contraction of ankle extensors might engage the distal tendon network and facilitate proximodistal energy transfer (*27*, *37*, *93*).

The BirdBot leg is a specific implementation of a geometric latch-mediated spring actuation mechanism, as defined by Longo and colleagues (*94*). A diverse range of animals use latch-mediated spring actuation to effectively control high-power, spring-mediated movements (*94*, *95*). In BirdBot, the distal bistable joint supports rapid disengagement of the stance leg spring, actuated by the leg angular rotation in stance. It results in a rapid release of stored energy, similar to the asymmetric joint power profile observed at the TMP joint in running turkeys (*62*). High ground clearance for swing is achieved through rapid, coupled flexion of joints upon clutch disengagement. A similar release of stored elastic energy occurs in horses' legs, triggered by rotation of the ground reaction force vector over leg joint axes, leading to a catapult-like mechanism (*28*). A complex but more direct replication of the tendon network in the horse leg has been recently implemented in a robot by (*96*). Such engagement and disengagement mechanisms enable automatic release of elastic energy over a range of locomotor frequencies and loading conditions, reducing the demand for actuator work and the need for rapid sensory feedback control.

Current legged robots often use direct joint actuation analogous to myotatic unit control, with extension and flexion by joint torque actuators. Transitions between swing and stance must actively be sensed and controlled, using contact, force, or proprioceptive sensors (*46*, *97*, *98*). Although this approach achieves smooth and stable gaits, it relies on precise and high-frequency sensor feedback to detect contact and impact events (*18*, *21*). Paradoxically, existing robots remain clumsy compared with animals, despite using appreciable faster sensing- and information-transfer rates (*22*). Sensor data can be noisy, making it hard to reliably detect contact events, particularly in unstructured terrain (*20*, *21*). To reliably detect contacts and control gait, many robots rely on control architectures that include hybrid feedforward/feedback, model-based prediction and learning strategies (*20*).

In contrast, BirdBot uses a single feedforward motor command at the proximal joint to coordinate complex leg actuation. BirdBot's leg clutch automatically engages and generates ground reaction forces upon loading and disengages upon unloading, without the need for sensors. BirdBot's stance spring passively deflects under load and rebounds after mid-stance, cycling elastic energy. Similar compliant leg robots can operate with no sensors and even stabilize after step-down perturbations (*76*, *99*). Thus, spring-leg designs not only minimize actuator work but can also simplify leg control.

As a consequence of BirdBot's underactuated design, gaits are not directly commanded. Instead, gaits emerge from the interaction between feedforward motor commands and ground reaction forces. This is illustrated by the discrepancy between commanded and observed duty factor. The commanded duty factor of the CPG-driven hip motor is 0.60 at a stride frequency of 1.5 Hz, and the observed gait duty factor is 0.49. This is similar to other robots with elastic legs and CPG control (*45*). Bipeds transition to running gaits at Froude numbers above 0.5 (*100*). BirdBot displayed a grounded gait at slower speed (0.50 m/s; Froude number Fr = 0.09) and brief aerial phases at higher speed, at a Froude number of 0.20 (0.75 m/s). We set the high-level CPG control parameters of amplitude, frequency, and duty factor, and the gait emerged from the robot's elastic leg mechanics.

The structure of Eq. 1 indicates no limitations in scaling BirdBot's leg mechanism to very large sizes. In Fig. 8, we show a large-scale demonstration with a hip height of 1.75 m that carries a human's weight. Once the foot joint j4 is digital-flexed, the knee joint j1 can be flexed without loading the leg's global spring (Fig. 8C). On the

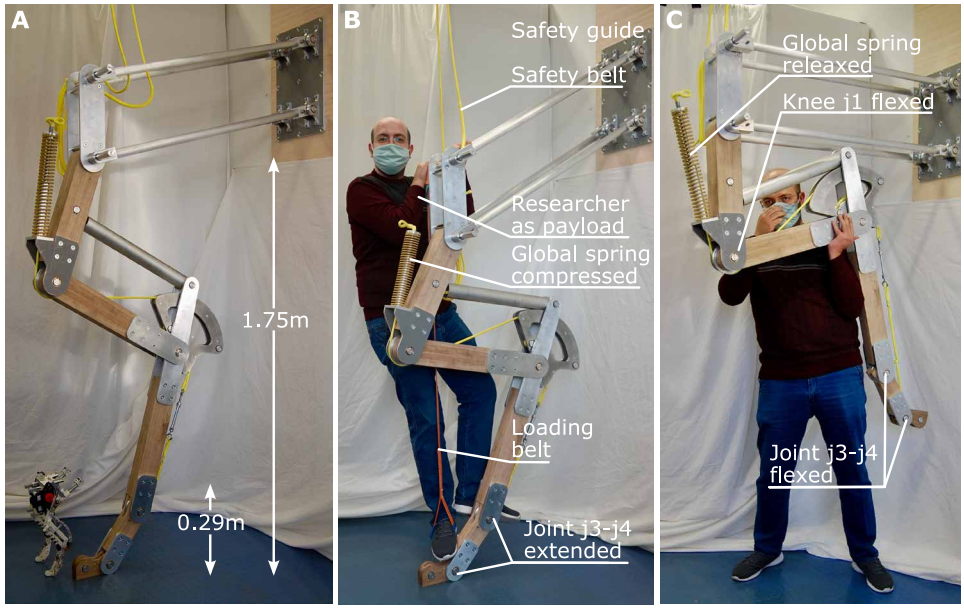

Fig. 8. Scalability of the BirdBot leg design. (**A**) Small-scale (0.29 m) and large-scale (1.75 m) versions of the BirdBot leg. (**B**) The large BirdBot leg supports the weight of a human, hanging by a belt on the hip joint axis. (**C**) With the distal leg digits flexed, the parallel leg spring is disengaged, and knee and ankle joints can be flexed without resistance from the GST.

basis of our analysis and physical demonstrations, we suggest that BirdBot's leg design can become a blueprint for large legged machines.

BirdBot's leg has no direct actuation for leg length extension. Nonsteady locomotion can demand net positive or negative work at distal joints (*6*, *37*, *93*, *101*, *102*). To increase BirdBot's versatility in rough terrain or to facilitate acceleration, a lightweight leg extension actuator could be placed in parallel with the distal extensor tendons (fig. S11). Additional actuators would not only increase versatility and robustness but also increase the leg mass, draw additional power and likely require more complex control with sensory feedback.

Clutch mechanisms, similar to that in BirdBot, need to be lightweight, robust, and of minimal complexity for mobile use in prosthetics, exoskeletons, and other legged robots. Loading conditions change rapidly, and clutches in the drive chain connect and disconnect external and internal forces, from zero to multiple body weights within tens of milliseconds (*103*, *104*). Wiggin *et al.* (*105*) designed a clutch for a human ankle joint exoskeleton that loads its spring in stance and releases the stored energy at push-off, freeing the ankle joint for the swing phase. van den Bogert (*47*) analyzed whole-leg multiarticular passive exoskeleton designs and found that they could substantially reduce joint moments and power; however, no geometry was found to enable a "clutch-like" function, with automatic switching from slack (in swing) to stiff (in stance) [page 6 of (*47*)]. Diller *et al.* (*106*) designed an active exoskeleton with a lightweight and efficient electrostatic adhesion clutch, which altered ankle joint stiffness by selectively engaging parallel rubber springs. Clutches have been integrated into soft exoskeletons, where they hold and release elastic belts (*107*). SPEAR robot's foot features a sprocket-like structure that interlocks with a chain section of a biarticular tendon in stance and disconnects the robot's knee in swing, allowing efficient forward hopping with slacked joints in swing (*108*). The multisegmented leg of FastRunner featured ankle and/or knee clutch mechanisms. Although the 1.4-m-tall FastRunner version did not run in hardware, its simulation reached fast speeds with a single, leg-angle actuator (Froude number Fr = 5 to 7; see table S1) (*109*–*111*). These findings suggest yet-untapped potential for effectively designed elastic clutches to improve robot performance. For future work, we suggest that a hybrid design with BirdBot's clutch mechanism combined with direct actuation and sensory feedback control could merge the benefits of both systems to achieve robust and versatile locomotion.

Recently, multiple advances have improved the economy and performance of legged robots. Robots designed with "quasi-direct" or "proprioceptive" actuation use strong, brushless motors and low-ratio gearboxes (*112*). In these robots, interjoint control is governed by an internal robot model, which matches inter- and intrajoint torque to work against external loads. Joint power is applied directly, with extensor and flexor actuation demanding negative and positive work as the leg compresses and extends. These robots can benefit from power regeneration during negative power phases and redistribute recouped power to other actuators or back into the battery (*17*, *112*).

Another approach is to use compliant legs with parallel or serial springs to cycle energy and reduce actuator work (*45*, *99*). Previous robots with pantograph, spring-loaded legs, and in-parallel knee flexing actuation (*45*, *99*) were designed as quadruped robots. Under feedforward control, Cheetah-cub achieved self-stable trot gait patterns with relatively high speeds (Froude number Fr = 1.3). However, without a disengagement mechanism, the stiff extensor spring requires large and rapid torques to shorten the leg for ground clearance in swing. Consequently, Cheetah-cub demanded high electrical power, resulting in a metabolic COT of 6.6 J/N·m, almost four times that of an animal of equal weight (Fig. 7C and table S1) (*45*, *76*).

BirdBot shares several features with Cheetah-cub, including spring-loaded legs, a proximal pantograph, small-sized, brushed-motor actuators, and a similar weight. BirdBot features an important improvement—its foot-triggered clutch slacks the leg joints during swing. With the stance spring disengaged, the knee torque required to flex the leg for ground clearance decreases from 3.7 N·m for a Cheetah-cub leg design to 0.1 N·m with a BirdBot leg (static loading conditions; table S5). BirdBot's distal tendon also stores energy in stance and releases it at the end of stance (Fig. 6B), similar to the ankle actuation of passive walkers (*57*). Both characteristics contribute to BirdBot's low COT—low knee-flexing torque and tendon elastic recoil of the distal tendon. As a result, BirdBot's COT—one-quarter that of Cheetah-cub—is within the range of an animal of equal weight.

Although comparing robots with different morphologies and numbers of legs is imprecise, it nonetheless provides a general perspective on how energetic performance can be improved by design. BirdBot, MIT Cheetah 3 (*113*), and SPEAR (*108*) cluster below the COT of natural runners (Fig. 7C). Hence, legged robots with power regeneration and low-ratio gearing can achieve exceptional energy economy (MIT Cheetah 3; table S1) (*113*, *114*). Specialized hopping robots can be especially economical, because they operate with a single leg angle actuator, achieving a relative COT of 45% (Fig. 7C and table S1) (*76*).

BirdBot's guidance system keeps the trunk from translating sideways and rotating in any direction. Hence, the trunk will not pitch if torque is applied (fig. S5). Immediately before swing-stance transition engagement, the robot's digits require clearance to rotate from digital-flexed to digital-extended. A forward pitching trunk could reduce ground clearance. To compensate for trunk pitching in an unguided version, higher clearance could be achieved by increasing leg angular velocity to reach an earlier maximum forward leg angle with its required posture for clutch-initialization. Implementing a fully three-dimensional version of BirdBot will also require dedicated actuation and control for balance correction to move in three-dimensional environments (*115*–*117*). In general, pitching moments can be reduced by supporting BirdBot's hip-powered actuation with actuator-powered leg extension, with dedicated designs (fig. S11). Alternatively, the robot's trunk design can be adapted for hip-only actuation (*118*).

Conclusion

Legged robot designers tend to neglect typologies and mechanisms observed in animal legs and often prefer high-powered actuation and relatively simple leg structures. Despite the limitations of biological tissues, the agile and robust performance of animals suggests that robot designs can benefit from a rigorous understanding of more complex multiarticular, strategically geared spring mechanisms to achieve simple, fast, and economic leg control. An additional benefit of the mechanism demonstrated here is the potential for more effective foot-substrate interactions. Many robots still use point-foot designs, which simplifies internal model computation. A clear advantage of the mechanism proposed here is its ability to stand upright, with all actuators switched off. The torque-loaded foot-segment creates a range of viable center of pressure points, where the robot's center of mass can be balanced above, reminiscent

of a flamingo standing while sleeping (Fig. 8A and fig. S2) (*30*). The functional implications of a foot acting as an effective leg-clutching mechanism in a multisegment elastic leg remain unexplored. The proposed mechanism allows rapid mechanical control of swing-stance transitions, which can be particularly beneficial for navigating uneven, unpredictable, or soft terrains. The leg clutch and foot segment enable rapid spring engagement and adjustment of the center of pressure in direct response to altered loading. Additional research is needed to understand how foot function contributes to locomotion in animals and to make effective use of foot-mediated control of legged robot locomotion.

MATERIALS AND METHODS

Robot prototype

BirdBot is designed to be left-right symmetric. The robot's design parameters are provided in table S2, and its design is shown in Fig. 3 (A and B). Most of the robot's trunk and leg parts are printed from Acrylonitrile Butadiene Styrene on a fused deposition printer (uPrint SE Plus). The nomenclature for segments and angles can be found in fig. S3. Each leg features two springs. The global spring is mounted serially to the global tendon. We simplify the mounting of force sensors and mount the global spring to the robot's trunk, instead of, for example, the leg segment s01 (fig. S3D). As a consequence, the GST also spans over joint j0. A second, pantograph spring (Fig. 3A) is mounted within the segment s12p. The pantograph spring exerts forces when both parts of segment s12p are pulled apart, for example, when leg retraction torque is exerted at the hip joint (*76*). Hence, the pantograph spring acts as a functional rotatory compliant element in response to hip torques. In emus, the gastrocnemius muscle is positioned similar to the spring-12p. Two off-the-shelf robot actuators (Dynamixel, MX-64 AT, RS485) actuate each leg; the hip actuator directly attaches to the leg and swings it forward (protraction) and backward (retraction). The knee actuator shortens the leg's knee joint j1 through the knee flexor tendon. Leg lengthening is not actively supported, meaning the leg lengthens fully after swing phase, only supported by gravity and the leg's angular momentum. The robot's hip axes and knee flexor pulleys are connected to the trunk by large-diameter, thin-section ball bearings. Low friction bushings guide the remaining joint axes, which are cut from steel stock material.

Spring tendon network

A network of four tendons and spring tendons is mounted to each leg, shown in Fig. 3B. The GST splits into a proximal and a distal part (red). The DFT supports j3 and leg disengagement (orange). The knee flexor tendon lifts the slack leg (blue). A last pair of tendons rotates both digits into digital extension (digit-1 extensor and digit-2 extensor, light and olive green). Each tendon is tensioned through a tendon adjustment mechanism (TAM; fig. S9). TAMs are custom-made, from a plastic worm gear driving a drum winding up the tendon, and work similar to a violin's string tensioning mechanism. The multiarticular GST extends joints j1 to j4 against loads in leg length direction during stance phase (Fig. 3B). The GST also spans over joint j0 to simplify mounting the spring's force sensor. The biarticular DFT runs parallel to the GST but spans only over the leg's two distal joints j3 and j4. When tensioned by joint j4 flexion through stance phase, the DFT pushes joint j3 from one stable joint position, over its unstable, collinear position of segment s23 and digit-1 (Fig. 5, C and D). The DFT action "collapses" joint j3 and with it the in-parallel mounted GST. The DFT does not insert into a spring; instead, we directly use the tendon's intrinsic elasticity, similar to a very stiff spring. We estimated the tendon's spring-like stiffness (k = 60 N/mm) in its built-in configuration. The knee flexor tendon flexes the knee joint j1. Its proximal end inserts into the knee actuator pulley. The tendon is then routed over the hip j0 axis, into the knee flexing pulley, and lastly into its TAM mounted to the s23 segment (tibiotarsus; Fig. 3B and fig. S3D). A pair of dorsiflexion tendons span over joints j2 to j4. When joint j2 extends just before touchdown (Fig. 3B), the dorsiflexion tendons rotate digit-1 and digit-2 into a digital-extended position. The dorsiflexion tendon TAMs are integrated into segment s23. The DFT and the GST are mounted antagonistically to the dorsiflexion tendons, and hence, we adjusted each tendons' slack carefully. All tendons are made from 1-mm-thick cables (Dyneema). Tendon ends are manually cut to length. The tendon's tail is inserted into the standing part of the tendon to create an eye. Both twines are lock-stitched together by hand.

The left and right leg GSTs were initially set to zero slack length, with the robot's legs in the air and all the leg segments extended. The robot was placed on the ground, and the GSTs were adjusted for an equal joint j1 angle between the left and the right leg. We adjusted the DFTs on the standing robot with femur segments set vertically by the hip actuator (joint j0, 0°). The tension of the DFTs was adjusted to a force of F = 100 N, just before the joint j3 snap-through. The knee flexor tendon's slack was removed with the femur segment positioned vertically. Both dorsiflexion tendons were adjusted to create joint j4 digital extension when joint j2 is extended. Knee and hip torque sensors and the GST force sensor were calibrated with an external load cell. The robot's legs were placed horizontally to avoid the effect of gravity. The tendon buckle sensor was calibrated with a defined external load pulling on the DFT.

Actuators and low-level actuator control

Four off-the-shelf robot actuators drive the robot's legs (Dynamixel, MX-64 AT; Fig. 3, A and B). One hip actuator per leg is mounted between the trunk and the femur segment s01; it directly moves the femur. The knee actuator flexes the knee joint j1 by pulling on the knee flexor tendon (Fig. 3B). We controlled the actuators in position mode, from a control PC with an update frequency of f = 125 Hz. All four actuators are connected through a single RS485 communication bus. A U2D2 universal serial bus (USB) communication converter connects the communication bus via USB to the control PC. We modified the MATLAB Dynamixel software development kit for this use (SDK, v.3.5.4). All control commands were sent as feedforward signals.

Instrumentation

Each leg is instrumented with four sensors measuring force or torque. A custom-designed sensor measures the hip actuator's reaction torque. The reaction force F is measured by an off-the-shelf beam-type load cell (TAL220; 100 N), at a lever arm length of l = 47 mm, and we calculate the hip reaction torque $\tau = F \cdot l$ (Fig. 6C). A second, identically constructed sensor measures the reaction torque of the knee actuator, and we calculate the torque acting at the knee flexor tendon (Fig. 6E). The GST's force is measured with an identical force sensor (fig. S9). We measure the DFT's force with a custom-designed tendon buckle sensor. All joint positions are measured with absolute magnetic encoders (AS 5045, AMS), recorded at f = 333 Hz,

and time-stamped with a microcontroller board (Arduino Mega), individually for the right and left leg. Both microcontrollers were connected to a PC with USB. Force data were sampled by a data acquisition system (cDAQ-9189, National Instruments) at $f = 1$ kHz, with strain bridge input modules (NI-9237). A custom-written LabVIEW program recorded the NI MAX module data, including the trigger line status. The current supplied to the actuators was captured with an external current sensor (LA 25, 25 A, LEM), mounted to a custom amplifier. The amplifier's voltage output signal was recorded with an analog-to-digital converter (NI-9205). The current sensor was calibrated with a 1-ohm precision resistor. Current data were time-stamped and trigger-synchronized. An external power supply provided the robot's actuator voltage (12.0 V) through a power cable.

Video

Gait experiments were recorded with a high-speed camera (MiroLab 110, Phantom) at a frame rate of $f = 400$ frames/s, and still frames were extracted from video material for Fig. 6A. High-speed videos were synchronized to the data on the basis of an optical and electrical trigger event. Touchdown and toe-off events were determined manually from high-speed videos. Further videos and photos were recorded with a camcorder (FDR-AX 100, Sony) and a digital camera (D5500, Nikon).

Calculation of Froude number, COT, and electrical and mechanical power

We calculate the Froude number as

$$\mathrm{Fr} = v^2/gl \tag{5}$$

according to (*119*), where v is the robot's speed v in meters per second on the treadmill, averaged over in the sum of 70 strides from five experiments with each 14 strides. The robot's standing hip height is $l = 0.29$ m, and the gravitational acceleration is $g = 9.81$ m/s^2. The mechanical power P (in watts) was calculated as the product of velocity v (in meters per second) and force F (in newtons), or angular velocity ω (in radian per second) and torque τ (in newton-meter). The robot's electrical (metabolic) COT was calculated according to (*120*). We measured the instantaneous current I (in amperes) with current clamps for each actuator individually, calibrated the data, and kept the positive values only, from 70 strides. We then summed up the data of the four actuators and derived the means and SD (table S4). We then calculated the net electrical COT

$$\mathrm{COT_{en}} = ((U \cdot I) - P_{\mathrm{SB}})/(m \cdot g \cdot v) \tag{6}$$

where we removed the standby actuator power $P_{\mathrm{SB}} = 4.8$ W. The actuator's manual specifies 100-mA standby current, which we confirmed by own measurement. The robot's weight mounted to the rail is $m = 1.73$ kg, the average robot speeds were $v = 0.50$ m/s at $f = 1$ Hz stride frequency, and $v = 0.75$ m/s for $f = 1.5$ Hz stride frequency. COT is normalized (in joules per newton-meter) to evaluate the energy efficiency during locomotion. However, animal locomotion data indicate that the COT decreases with increasing animal mass m, also shown with the "natural runner" down-sloping trend line in (*120*). To compare BirdBot's COT to legged hoppers, bipedal robots, and quadrupedal robots of different body masses, we first digitized Tucker's trend line [figure 2 of (*120*)], which leads to the following COT reference line (Fig. 7C, 100% line)

$$\log_{10}(\mathrm{COT_{nr}}) = -0.3138 \cdot \log_{10}(m) + 0.2346 \tag{7}$$

We added indicator lines (25, 50, 100, 200, and 400%) for a "relative COT" (in percentage), calculated as the ratio between the natural runner's COT and the robot's electrical net or total COT to Fig. 7C, to indicate COT grouping of robots of different types and sizes

$$\mathrm{COT_{re}} = \frac{\mathrm{COT_{nr}}}{\mathrm{COT_{en}}} \cdot 100\% \tag{8}$$

The above COT comparison is based on allometric relationships; we are comparing BirdBot with an average animal of the same body weight. Specific costs of transport values of similar sized birds at similar locomotion speeds are 0.81 J/N·m [guineafowl (*Numida meleagris*), 1.5 kg, between 0.5 and 3 m/s] (*121*), 1.30 J/N·m [leghorns (*Gallus gallus domesticus*), 2.0 kg, 0.7 m/s] (*122*), and 1.4 and 2.0 J/N·m (guineafowl, 1.3 kg, 0.5 and 1.0 m/s) (*123*).

Locomotion control pattern generation

We generated locomotion control patterns with a CPG, similar to (*45*, *124*). We applied CPG control to generate smooth hip joint angle trajectories, which is important when initializing the gait patterns. Custom-designed CPGs require only few driving parameters, such as amplitude, offset, phase shift, and duty factor. The CPG was implemented on a PC in MATLAB; the trajectories were sent to the actuators as feedforward signals. Stride frequencies of $f = 1.0$ and 1.5 Hz were set, resulting in robot speeds of 0.50 and 0.75 m/s, respectively. The left and the right leg received phase-shifted but otherwise identical trajectories

$$\dot{\phi}_i = 2\pi f + \sum_{i \neq j} c_{ij} \sin(\phi_j - \phi_i - \varphi_{ij}) \tag{9}$$

$$\dot{a}_i^h = \alpha(A_i^h - a_i^h) \tag{10}$$

$$\dot{o}_i^h = \alpha(O_i^h - o_i^h) \tag{11}$$

where ϕ_i is the i-oscillator's phase; $c_{12} = 1$ and $c_{21} = 0$ are coupling terms; f is the stride frequency, $\varphi_{12} = \pi$ and $\varphi_{21} = 0$ are phase shifts between the hip oscillators, a^h and A^h are the instantaneous and the commanded hip amplitude, respectively; o^h and O^h are the instantaneous and the commanded hip offset, respectively; and α is a convergence gain. The commanded duty factor D adapts the phase Θ_i^h of the hip joint of leg i, leading to the hip actuator set position h_i

$$\Theta_i^h = \begin{cases} \dfrac{\phi_i}{2D} & 0 \leq \phi_i \leq 2\pi D \\ \dfrac{\phi_i + 2\pi(1-2D)}{2(1-D)} \end{cases} \tag{12}$$

$$h_i = a_i^h \cos(\Theta_i^h) + o_i^h \tag{13}$$

The active shortening of the leg length by the knee actuator is coupled to the hip oscillator's phase ϕ_i by the phase shift S_F (begin, flexing) and S_E (end, release and passive extension)

$$S_F = 2\pi S_f(1 - D) \tag{14}$$

$$S_E = 2\pi S_e(1 - D) \tag{15}$$

Table 1. The CPG parameters for gait 1 (f = 1 Hz) and gait 2 (f = 1.5 Hz).

Parameter	Gait 1	Gait 2	Parameter	Gait 1	Gait 2
f (Hz)	1	1.5	D_{vir}	0.6	0.6
A^h (°)	32	35	α	1	1
O^h (°)	22	30	S_f	0	0
A^k (°)	120	120	S_e	0.22	0.22

where S_F and S_e are the fraction of flexion and extension delay of swing phase, respectively. The knee i actuator angle is set as k_i, with the commanded knee amplitude A^k

$$k_i = \begin{cases} 0 & 0 \le \phi_i \le 2\pi D + S_F \\ A_i^k & 2\pi D + S_F \le \phi_i \le 2\pi - S_E \end{cases} \quad (16)$$

We observe that the commanded duty factor (D = 0.60) differs from the observed duty factor (D = 0.49, f = 1.5 Hz stride frequency). A typical CPG output for one stride of a single leg is provided in fig. S1. CPG parameters are provided in Table 1.

Cadaver studies

Emu cadavers were obtained from a prior study of emu ontogenetic biomechanics (*125*) at the Royal Veterinary College (RVC) Structure and Motion Laboratory. The animals were housed and reared at the RVC, and all procedures and humane euthanasia were conducted with ethical approval under a U.K. Home Office license: PPL707122. Cadavers were stored in a −20°C freezer after euthanasia and thawed slowly to room temperature before experiments.

Treadmill and guide setup

The robot walked on a recreational treadmill (model Christopeit TM500S), modified for speed control by setting a directly connected power supply voltage. The treadmill's speed was measured by a custom mounted encoder (AS 5045, AMS) and recorded by a microcontroller (Arduino Mega). A linear guide (Misumi SVR) was degreased and loosened for minimal sliding friction. The slider is mounted to an overhead rail, h = 0.53 m above the belt. Rail and robot are connected by a parallel four-bar guide, with segment lengths l = 0.51 m and l = 0.04 m. The rail and four-bar restrict the robot to translations in the sagittal plane (fore-aft and up-down) and prohibit trunk pitching. The linear guide's position is measured by a pair of countermounted draw-wire sensors (Waycon LX-PA-20), read out by an analog-digital converter (NI 9205).

Static knee joint torque in swing and stance

For static conditions, we calculated the torque required to extend the knee joint when standing on a single leg and holding the robot's weight and while lifting the lower leg. We simulated three different robot spring and actuator configurations (fig. S4, A to C). All three modeled robot configurations have an equal mass of m = 1.73 kg, identical to BirdBot. The robots' center of mass and their hip joints align vertically, and no hip torque is induced during standing. In the lifted leg scenario, the lower leg mass and the horizontal distance between its segments' center of gravity and the knee joint are assumed to be identical for all three designs (m_{lower} = 0.092 kg, l_{distance} = 0.056 m).

Single leg disengagement experiment

The joint positions at leg disengagement and leg unloading were determined on the basis of visual cues, tracked manually from high-speed video footage. Angles were extracted in ImageJ software. The virtual leg angle was defined by the joints j0 and j4 and a third point at the trunk. For the leg with the DFT mounted, we determined the disengagement leg angle when $\alpha_{j3} > 180°$.

Disengagement tendon work calculation

We estimate a spring-like behavior of the DFT. We calculated the tendon's stiffness (k_{DET}) by measuring a known tendon force F_{DET} and the tendon's change in length $\Delta(l_{\text{DET}})$, in its built-in state. For the plot Fig. 6B, we calculate the DFT work W_{DET} from the recorded tendon force, and the change of tendon length l_{DET} wrapping around the pulleys of joints j3 and j4

$$W_{\text{DET}} = \frac{1}{2} F_{\text{DET}} \cdot \Delta l_{\text{DET}} \quad (17)$$

GST work calculation

The work W_{GST} of the GST is calculated from the tendon's force, which is identical to the spring force, and the spring stiffness (Fig. 6D)

$$W_{\text{GST}} = \frac{1}{2} \frac{F_{\text{GST}}^2}{k} \quad (18)$$

Data processing

Data were processed in MATLAB (MathWorks). Joint speeds were derived from joint encoder data, applying the "sgolay_t" MATLAB function to joint position data (author: T. Ramos, settings: N = 4, F = 51, DIM = 1). Current data were filtered with a zero-phase digital filter (30-Hz low pass, second order, 0.2 PassbandRipple).

Statistics

Unless otherwise indicated, uncertainty bounds are provided as means and SD (means ± SD). Data from continuous data plots are presented as means and 95% CI (means ± CI), averaged over 70 strides. Single leg disengagement data are presented as mean of 20 repetitions per leg configuration. Mean disengagement angles of 69.0° ± 1.2° and 59.0° ± 0.3° (means ± SD) were recorded for the leg with and without the DFT, respectively (Fig. 5). The 10° difference was statistically

significant according to a Mann-Whitney U test, $n1 = n2 = 20$, $P = 0.01$. Correlation coefficients for j2 and j3 joint trajectories (Fig. 2) were calculated as r = correff(j2, j3) (MATLAB), with 2001 data points from five joint extensions and flexions. The flexion correlation coefficient is $r_{flex} = 0.99$, and the extension correlation coefficient is $r_{ext} = 0.96$ (Fig. 2C). Correlation coefficients $r > 0.8$ are considered an indicator for strong coupling.

SUPPLEMENTARY MATERIALS

www.science.org/doi/10.1126/scirobotics.abg4055
Text S1 to S5
Figs. S1 to S14
Tables S1 to S5
Movies S1 to S7
References (*127*–*133*)

REFERENCES AND NOTES

1. J. Delmerico, S. Mintchev, A. Giusti, B. Gromov, K. Melo, T. Horvat, C. Cadena, M. Hutter, A. Ijspeert, D. Floreano, L. M. Gambardella, R. Siegwart, D. Scaramuzza, The current state and future outlook of rescue robotics. *J. Field Robot.* **36**, 1171–1191 (2019).
2. F. Iida, A. J. Ijspeert, Biologically inspired robotics, in *Springer Handbook of Robotics* (Springer, 2016), chap. 75, pp. 2015–2034.
3. N. Kashiri, A. Abate, S. J. Abram, A. Albu-Schaffer, P. J. Clary, M. Daley, S. Faraji, R. Furnemont, M. Garabini, H. Geyer, A. M. Grabowski, J. Hurst, J. Malzahn, G. Mathijssen, D. Remy, W. Roozing, M. Shahbazi, S. N. Simha, J. B. Song, N. Smit-Anseeuw, S. Stramigioli, B. Vanderborght, Y. Yesilevskiy, N. Tsagarakis, An overview on principles for energy efficient robot locomotion. *Front. Roboti. AI* **5**, 129 (2018).
4. G.-Z. Yang, J. Bellingham, P. E. Dupont, P. Fischer, L. Floridi, R. Full, N. Jacobstein, V. Kumar, M. McNutt, R. Merrifield, B. J. Nelson, B. Scassellati, M. Taddeo, R. Taylor, M. Veloso, Z. L. Wang, R. Wood, The grand challenges of Science Robotics. *Sci. Robot.* **3**, eaar7650 (2018).
5. K. Nishikawa, A. A. Biewener, P. Aerts, A. N. Ahn, H. J. Chiel, M. A. Daley, T. L. Daniel, R. J. Full, M. E. Hale, T. L. Hedrick, A. K. Lappin, T. R. Nichols, R. D. Quinn, R. A. Satterlie, B. Szymik, Neuromechanics: An integrative approach for understanding motor control. *Integr. Comparative Biol.* **47**, 16–54 (2007).
6. M. A. Daley, Understanding the agility of running birds: Sensorimotor and mechanical factors in avian bipedal locomotion. *Integr. Comparative Biol.* **58**, 884–893 (2018).
7. L. H. Ting, H. J. Chiel, R. D. Trumbower, J. L. Allen, J. L. McKay, M. E. Hackney, T. M. Kesar, Neuromechanical principles underlying movement modularity and their implications for rehabilitation. *Neuron* **86**, 38–54 (2015).
8. L. H. Ting, H. J. Chiel, Muscle, biomechanics, and implications for neural control. *Neurobiol. Motor Control. Fund. Concepts New Direct.* 365–416 (2017).
9. M. Plooij, G. Mathijssen, P. Cherelle, D. Lefeber, B. Vanderborght, Lock your robot: A review of locking devices in robotics. *IEEE Robot. Autom. Mag.* **22**, 106–117 (2015).
10. H. L. More, J. R. Hutchinson, D. F. Collins, D. J. Weber, S. K. H. Aung, J. M. Donelan, Scaling of sensorimotor control in terrestrial mammals. *Proc. R. Soc. B Biol. Sci.* **277**, 3563–3568 (2010).
11. T. R. Nichols, T. C. Cope, T. A. Abelew, 8 rapid spinal mechanisms of motor coordination. *Exerc. Sport Sci. Rev.* **27**, 255–284 (1999).
12. R. Poppele, C. Terzuolo, Myotatic reflex: Its input-output relation. *Science* **159**, 743–745 (1968).
13. A. A. Sharp, E. Ma, A. Bekoff, Developmental changes in leg coordination of the chick at embryonic days 9, 11, and 13: Uncoupling of ankle movements. *J. Neurophysiol.* **82**, 2406–2414 (1999).
14. Y. P. Ivanenko, R. E. Poppele, F. Lacquaniti, Five basic muscle activation patterns account for muscle activity during human locomotion. *J. Physiol.* **556**, 267–282 (2004).
15. S. Aoi, T. Ohashi, R. Bamba, S. Fujiki, D. Tamura, T. Funato, K. Senda, Y. Ivanenko, K. Tsuchiya, Neuromusculoskeletal model that walks and runs across a speed range with a few motor control parameter changes based on the muscle synergy hypothesis. *Sci. Rep.* **9**, 369 (2019).
16. L. Righetti, J. Buchli, M. Mistry, M. Kalakrishnan, S. Schaal, Optimal distribution of contact forces with inverse-dynamics control. *Int. J. Rob. Res.* **32**, 280–298 (2013).
17. C. Hubicki, J. Grimes, M. Jones, D. Renjewski, A. Spröwitz, A. Abate, J. Hurst, ATRIAS: Design and validation of a tether-free 3D-capable spring-mass bipedal robot. *Int. J. Rob. Res.* **35**, 1497–1521 (2016).
18. S. Seok, A. Wang, D. Otten, S. Kim, Actuator design for high force proprioceptive control in fast legged locomotion, in *Proceedings of the 2012 IEEE/RSJ International Conference on Intelligent Robots and Systems (IROS)* (IEEE, 2012), pp. 1970–1975.
19. D. J. Hyun, S. Seok, J. Lee, S. Kim, High speed trot-running: Implementation of a hierarchical controller using proprioceptive impedance control on the MIT Cheetah. *Int. J. Rob. Res.* **33**, 1417–1445 (2014).
20. G. Bledt, P. M. Wensing, S. Ingersoll, S. Kim, Contact model fusion for event-based locomotion in unstructured terrains, in *Proceedings of the 2018 IEEE International Conference on Robotics and Automation (ICRA)* (IEEE, 2018), pp. 4399–4406.
21. F. Grimminger, A. Meduri, M. Khadiv, J. Viereck, M. Wüthrich, M. Naveau, V. Berenz, S. Heim, F. Widmaier, T. Flayols, J. Fiene, A. Badri-Spröwitz, L. Righetti, An open torque-controlled modular robot architecture for legged locomotion research. *IEEE Robot. Autom. Lett.* **5**, 3650–3657 (2020).
22. M. S. Ashtiani, A. Aghamaleki Sarvestani, A. Badri-Spröwitz, Hybrid parallel compliance allows robots to operate with sensorimotor delays and low control frequencies. *Front. Robot. AI* **8**, 645748 (2021).
23. N. U. Schaller, thesis, University of Heidelberg (2008).
24. N. U. Schaller, B. Herkner, R. Villa, P. Aerts, The intertarsal joint of the ostrich (*Struthio camelus*): Anatomical examination and function of passive structures in locomotion. *J. Anat.* **214**, 830–847 (2009).
25. M. A. Daley, A. Voloshina, A. A. Biewener, The role of intrinsic muscle mechanics in the neuromuscular control of stable running in the guinea fowl. *J. Physiol.* **587**, 2693–2707 (2009).
26. M. A. Daley, A. A. Biewener, Running over rough terrain reveals limb control for intrinsic stability. *Proc. Natl. Acad. Sci. U.S.A.* **103**, 15681–15686 (2006).
27. M. A. Daley, G. Felix, A. A. Biewener, Running stability is enhanced by a proximo- distal gradient in joint neuromechanical control. *J. Exp. Biol.* **210**, 383–394 (2007).
28. A. M. Wilson, J. C. Watson, G. A. Lichtwark, A catapult action for rapid limb protraction. *Nature* **421**, 35–36 (2003).
29. M. P. McGuigan, A. M. Wilson, The effect of gait and digital flexor muscle activation on limb compliance in the forelimb of the horse Equus caballus. *J. Exp. Biol.* **206**, 1325–1336 (2003).
30. Y.-H. Chang, L. H. Ting, Mechanical evidence that flamingos can support their body on one leg with little active muscular force. *Biol. Lett.* **13**, 20160948 (2017).
31. J.-M. Denoix, J.-P. Pailloux, *Physiotherapie und Massage bei Pferden Bewegungstherapie nach den Gesetzen der Biomechanik ; 4 Tabellen* (Stuttgart: Ulmer, 2000).
32. R. Pfeifer, M. Lungarella, F. Iida, Self-organization, embodiment, and biologically inspired robotics. *Science* **318**, 1088–1093 (2007).
33. H. Elftman, The function of muscles in locomotion. *Am. J. Physiol. Leg. Content* **125**, 357–366 (1939).
34. G. J. van Ingen Schenau, M. F. Bobbert, R. H. Rozendal, The unique action of bi-articular muscles in complex movements. *J. Anat.* **155**, 1–5 (1987).
35. G. Jan Van Ingen Schenau, On the action of bi-articular muscles, a review. *Nethe. J. Zool.* **40**, 521–543 (1989).
36. A. D. Kuo, The action of two-joint muscles: The legacy of WP Lombard, in *Classics in Movement Science* (Human Kinetics, 2001), pp. 289–316.
37. M. A. Daley, A. A. Biewener, Leg muscles that mediate stability: Mechanics and control of two distal extensor muscles during obstacle negotiation in the guinea fowl. *Philos. Trans. R. Soc. B Biol. Sci.* **366**, 1580–1591 (2011).
38. J. C. Gordon, N. C. Holt, A. Biewener, M. A. Daley, Tuning of feedforward control enables stable muscle force-length dynamics after loss of autogenic proprioceptive feedback. *eLife* **9**, e53908 (2020).
39. A. J. Ijspeert, Biorobotics: Using robots to emulate and investigate agile locomotion. *Science* **346**, 196–203 (2014).
40. W. P. Lombard, The tendon action and leverage of two-joint muscles of the hind leg of the frog, with special reference to the spring movement. *Contributions to medical research. Wahr, Ann Arbor* (1903), pp. 280–301.
41. M. Hildebrand, The mechanics of horse legs. *Am. Sci.* 594–601 (1987).
42. K. Arikawa, S. Hirose, Development of quadruped walking robot TITAN-VIII, in *Proceedings of the 1996 IEEE/RSJ International Conference on Intelligent Robots and Systems '96 (IROS 96)* (IEEE, 1996), vol. 1, pp. 208–214.
43. H. Witte, R. Hackert, K. Lilje, N. Schilling, D. Voges, G. Klauer, W. Ilg, J. Albiez, A. Seyfarth, D. Germann, M. Hiller, R. Dillmann, M. Fischer, Transfer of biological principles into the construction of quadruped walking machines, in *Proceedings of the Second International Workshop on Robot Motion and Control* (IEEE, 2001), pp. 245–249.
44. D. C. Kar, Design of statically stable walking robot: A review. *J. Robot. Syst.* **20**, 671–686 (2003).
45. A. Spröwitz, A. Tuleu, M. Vespignani, M. Ajallooeian, E. Badri, A. Ijspeert, Towards dynamic trot gait locomotion: Design, control and experiments with Cheetah-cub, a compliant quadruped robot. *Int. J. Robot. Res.* **32**, 932–950 (2013).
46. S. Seok, A. Wang, M. Y. Chuah, D. Otten, J. Lang, S. Kim, Design principles for highly efficient quadrupeds and implementation on the MIT Cheetah robot, in *Proceedings of the 2013 IEEE International Conference on Robotics and Automation* (IEEE, 2013), pp. 3307–3312.
47. A. J. van den Bogert, Exotendons for assistance of human locomotion. *Biomed. Eng. Online* **2**, 17 (2003).

48. J. Pratt, G. Pratt, Intuitive control of a planar bipedal walking robot, in *Proceedings of the IEEE International Conference on Robotics and Automation (ICRA '98)* (IEEE, 1998), vol. 3, pp. 1–12.
49. R. M. Alexander, H. C. Bennet-Clark, Storage of elastic strain energy in muscle and other tissues. *Nature* **265**, 114–117 (1977).
50. R. M. Alexander, Elastic energy stores in running vertebrates. *Am. Zool.* **24**, 85–94 (1984).
51. T. A. McMahon, The role of compliance in mammalian running gaits. *J. Exp. Biol.* **115**, 263–282 (1985).
52. A. Ananthanarayanan, M. Azadi, S. Kim, Towards a bio-inspired leg design for high-speed running. *Bioinspir. Biomim.* **7**, 046005 (2012).
53. K. Kurokawa, R. Sato, S. Hiasa, A. Ming, F. Meng, H. Liu, X. Fan, X. Chen, Z. Yu, Q. Huang, Introduction of toe mechanism with bi-articular tendon into legged robot, in *Proceedings of the 2018 IEEE International Conference on Mechatronics and Automation (ICMA)* (IEEE, 2018), pp. 1597–1602.
54. W. Roozing, Z. Li, D. Caldwell, N. Tsagarakis, Design optimisation and control of compliant actuation arrangements in articulated robots for improved energy efficiency. *IEEE Robot. Autom. Lett.* **1**, 1110–1117 (2016).
55. H. Barazesh, M. Ahmad Sharbafi, A biarticular passive exosuit to support balance control can reduce metabolic cost of walking. *Bioinspir. Biomim.* **15**, 036009 (2020).
56. T. McGeer, Passive dynamic walking. *Int. J. Rob. Res.* **9**, 62–82 (1990).
57. S. Collins, A. Ruina, R. Tedrake, M. Wisse, Efficient bipedal robots based on passive-dynamic walkers. *Science* **307**, 1082–1085 (2005).
58. R. Tedrake, T. W. Zhang, M.-f. Fong, H. S. Seung, Actuating a simple 3D passive dynamic walker, in *Proceedings of the IEEE International Conference on Robotics and Automation, ICRA'04. 2004* (IEEE, 2004), vol. 5, pp. 4656–4661.
59. S. H. Collins, M. Wisse, A. Ruina, A Three-dimensional passive-dynamic walking robot with two legs and knees. *Int. J. Rob. Res.* **20**, 607–615 (2001).
60. S. Collins, A. Ruina, A bipedal walking robot with efficient and human-like gait, in *Proceedings of the 2005 IEEE International Conference on Robotics and Automation, ICRA 2005* (IEEE, 2005), pp. 1983–1988.
61. G. E. Weissengruber, G. Forstenpointner, D. Gangl, Gut zu Fuß - funktionell-anatomische Aspekte des bipeden Laufens beim Afrikanischen Strauß (*Struthio camelus* Linné, 1758). *Vet. Med. Austria* **90**, 67–78 (2003).
62. T. J. Roberts, J. A. Scales, Adjusting muscle function to demand: Joint work during acceleration in wild turkeys. *J. Exp. Biol.* **207**, 4165–4174 (2004).
63. J. Rubenson, D. G. Lloyd, T. F. Besier, D. B. Heliams, P. A. Fournier, Running in ostriches (*Struthio camelus*): Three-dimensional joint axes alignment and joint kinematics. *J. Exp. Biol.* **210**, 2548–2562 (2007).
64. P. J. Bishop, K. B. Michel, A. Falisse, A. R. Cuff, V. R. Allen, F. D. Groote, J. R. Hutchinson, Computational modelling of muscle fibre operating ranges in the hindlimb of a small ground bird (*Eudromia elegans*), with implications for modelling locomotion in extinct species. *PLOS Comput. Biol.* **17**, e1008843 (2021).
65. J. Rubenson, D. G. Lloyd, D. B. Heliams, T. F. Besier, P. A. Fournier, Adaptations for economical bipedal running: The effect of limb structure on three-dimensional joint mechanics. *J. R. Soc. Interface* **8**, 740–755 (2011).
66. A. Abourachid, E. Höfling, The legs: A key to bird evolutionary success. *J. Ornithol.* **153**, 193–198 (2012).
67. J. R. Hutchinson, J. W. Rankin, J. Rubenson, K. H. Rosenbluth, R. A. Siston, S. L. Delp, Musculoskeletal modelling of an ostrich (*Struthio camelus*) pelvic limb: Influence of limb orientation on muscular capacity during locomotion. *PeerJ* **3**, e1001 (2015).
68. N. Smith, A. Wilson, K. Jespers, R. Payne, Muscle architecture and functional anatomy of the pelvic limb of the ostrich (*Struthio camelus*). *J. Anat.* **209**, 765–779 (2006).
69. J. Gray, Studies in the mechanics of the tetrapod skeleton. *J. Exp. Biol.* **20**, 88–116 (1944).
70. M. S. Fischer, N. Schilling, M. Schmidt, D. Haarhaus, H. Witte, Basic limb kinematics of small therian mammals. *J. Exp. Biol.* **205**, 1315–1338 (2002).
71. H. Witte, J. Biltzinger, R. Hackert, N. Schilling, M. Schmidt, C. Reich, M. S. Fischer, Torque patterns of the limbs of small therian mammals during locomotion on flat ground. *J. Exp. Biol.* **205**, 1339–1353 (2002).
72. A. A. Biewener, Scaling body support in mammals: Limb posture and muscle mechanics. *Science* **245**, 45–48 (1989).
73. R. Blickhan, The spring-mass model for running and hopping. *J. Biomech.* **22**, 1217–1227 (1989).
74. T. A. McMahon, G. C. Cheng, The mechanics of running: How does stiffness couple with speed? *J. Biomech.* **23**, 65–78 (1990).
75. C. Farley, J. Glasheen, T. McMahon, Running springs: Speed and animal size. *J. Exp. Biol.* **185**, 71–86 (1993).
76. F. Ruppert, A. Badri-Spröwitz, Series elastic behavior of biarticular muscle-tendon structure in a robotic leg. *Front. Neurorobot.* **13**, 64 (2019).
77. E. Mahdy, M. Raouf, Normal anatomical and diagnostic imaging techniques of the musculotendinous structures of the ostrich (*Struthio camelus*) foot. *J. Adv. Vet. Anim. Res.* **7**, 242–252 (2020).
78. S. N. Patek, B. N. Nowroozi, J. E. Baio, R. L. Caldwell, A. P. Summers, Linkage mechanics and power amplification of the mantis shrimp's strike. *J. Exp. Biol.* **210**, 3677–3688 (2007).
79. M. A. Fedak, H. J. Seeherman, Reappraisal of energetics of locomotion shows identical cost in bipeds and quadrupeds including ostrich and horse. *Nature* **282**, 713–716 (1979).
80. R. L. Marsh, D. J. Ellerby, H. T. Henry, J. Rubenson, The energetic costs of trunk and distal-limb loading during walking and running in guinea fowl *Numida meleagris*: I. Organismal metabolism and biomechanics. *J. Exp. Biol.* **209**, 2050–2063 (2006).
81. D. J. Ellerby, M. Cleary, R. L. Marsh, C. I. Buchanan, Measurement of maximum oxygen consumption in guinea fowl *Numida meleagris* indicates that birds and mammals display a similar diversity of aerobic scopes during running. *Physiol. Biochem. Zool.* **76**, 695–703 (2003).
82. J. Rubenson, D. B. Heliams, D. G. Lloyd, P. A. Fournier, Gait selection in the ostrich: Mechanical and metabolic characteristics of walking and running with and without an aerial phase. *Proc. R. Soc. Lond. B Biol. Sci.* **271**, 1091–1099 (2004).
83. A. V. Birn-Jeffery, C. M. Hubicki, Y. Blum, D. Renjewski, J. W. Hurst, M. A. Daley, Don't break a leg: Running birds from quail to ostrich prioritise leg safety and economy on uneven terrain. *J. Exp. Biol.* **217**, 3786–3796 (2014).
84. R. M. Alexander, G. M. O. Maloiy, R. Njau, A. S. Jayes, Mechanics of running of the ostrich (*Struthio camelus*). *J. Zool. Lond.* **187**, 169–178 (1979).
85. M. A. Daley, A. J. Channon, G. S. Nolan, J. Hall, Preferred gait and walk–run transition speeds in ostriches measured using GPS-IMU sensors. *J. Exp. Biol.* **219**, 3301–3308 (2016).
86. Y. Blum, H. R. Vejdani, A. V. Birn-Jeffery, C. M. Hubicki, J. W. Hurst, M. A. Daley, Swing-leg trajectory of running guinea fowl suggests task-level priority of force regulation rather than disturbance rejection. *PLOS ONE* **9**, e100399 (2014).
87. D. Gangl, G. E. Weissengruber, M. Egerbacher, G. Forstenpointner, Anatomical description of the muscles of the pelvic limb in the ostrich (*Struthio camelus*). *Anat. Histol. Embryol.* **33**, 100–114 (2004).
88. R. Zhang, Q. Ji, G. Luo, S. Xue, S. Ma, J. Li, L. Ren, Phalangeal joints kinematics during Ostrich (*Struthio camelus*) locomotion. *PeerJ* **4**, e2324v1 (2016).
89. V. R. Allen, R. E. Kambic, S. M. Gatesy, J. R. Hutchinson, Gearing effects of the patella (knee extensor muscle sesamoid) of the helmeted guineafowl during terrestrial locomotion. *J. Zool.* 178–187 (2017).
90. N. S. Bradley, A. Bekoff, Development of coordinated movement in chicks: I. Temporal analysis of hindlimb muscle synergies at embryonic days 9 and 10. *Dev. Psychobiol.* **23**, 763–782 (1990).
91. J. C. Gordon, J. W. Rankin, M. A. Daley, How do treadmill speed and terrain visibility influence neuromuscular control of guinea fowl locomotion? *J. Exp. Biol.* **218**, 3010–3022 (2015).
92. S. M. Gatesy, Guineafowl hind limb function. II: Electromyographic analysis and motor pattern evolution. *J. Morphol.* **240**, 127–142 (1999).
93. T. J. Roberts, R. L. Marsh, P. G. Weyand, C. R. Taylor, Muscular force in running turkeys: The economy of minimizing work. *Science* **275**, 1113–1115 (1997).
94. S. Longo, S. Cox, E. Azizi, M. Ilton, J. Olberding, R. St Pierre, S. Patek, Beyond power amplification: Latch-mediated spring actuation is an emerging framework for the study of diverse elastic systems. *J. Exp. Biol.* **222**, jeb197889 (2019).
95. S. W. Lipfert, M. Günther, D. Renjewski, A. Seyfarth, Impulsive ankle push-off powers leg swing in human walking. *J. Exp. Biol.* **217**, 1218–1228 (2014).
96. K. Miyashita, Y. Masuda, M. Gunji, A. Fukuhara, K. Tadakuma, M. Ishikawa, Emergence of swing-to-stance transition from interlocking mechanism in horse hindlimb, in *Proceedings of the 2020 IEEE/RSJ International Conference on Intelligent Robots and Systems (IROS)* (IEEE, 2021), pp. 7860–7865.
97. C. Semini, N. G. Tsagarakis, E. Guglielmino, M. Focchi, F. Cannella, D. G. Caldwell, Design of HyQ—A hydraulically and electrically actuated quadruped robot. *Proc. Inst. Mech. Eng. I J. Syst. Control Eng.* **225**, 831–849 (2011).
98. M. Hutter, C. Gehring, D. Jud, A. Lauber, C. D. Bellicoso, V. Tsounis, J. Hwangbo, K. Bodie, P. Fankhauser, M. Bloesch, R. Diethelm, S. Bachmann, A. Melzer, M. A. Höepflinger, ANYmal - a highly mobile and dynamic quadrupedal robot, in *Proceedings of the 2016 IEEE/RSJ International Conference on Intelligent Robots and Systems (IROS)* (IEEE, 2016), pp. 38–44.
99. A. Spröwitz, A. Tuleu, M. Ajallooeian, M. Vespignani, R. Möckel, P. Eckert, M. D'Haene, J. Degrave, A. Nordmann, B. Schrauwen, J. Steil, A. J. Ijspeert, Oncilla robot: A versatile open-source quadruped research robot with compliant pantograph legs. *Front. Robot. AI* **5**, 67 (2018).
100. S. Gatesy, A. Biewener, Bipedal locomotion: Effects of speed, size and limb posture in birds and humans. *J. Zool.* **224**, 127–147 (1991).
101. T. J. Roberts, E. Azizi, Flexible mechanisms: The diverse roles of biological springs in vertebrate movement. *J. Exp. Biol.* **214**, 353–361 (2011).

102. J. W. Rankin, J. Rubenson, J. R. Hutchinson, Inferring muscle functional roles of the ostrich pelvic limb during walking and running using computer optimization. *J. R. Soc. Interface* **13**, 20160035 (May 2016).
103. E. J. Rouse, L. M. Mooney, H. M. Herr, Clutchable series-elastic actuator: Implications for prosthetic knee design. *Int. J. Rob. Res.* **33**, 1611–1625 (2014).
104. M. Plooij, M. Wisse, H. Vallery, Reducing the energy consumption of robots using the bidirectional clutched parallel elastic actuator. *IEEE Trans. Robot.* **32**, 1512–1523 (2016).
105. M. Wiggin, G. Sawicki, S. Collins, presented at the 2011 IEEE International Conference on Rehabilitation Robotics (ICORR) (IEEEE, 2011), pp. 1–5.
106. S. Diller, C. Majidi, S. H. Collins, A lightweight, low-power electroadhesive clutch and spring for exoskeleton actuation, in *Proceedings of the 2016 IEEE International Conference on Robotics and Automation (ICRA)* (IEEE, 2016), pp. 682–689.
107. C. Di Natali, A. Sadeghi, A. Mondini, E. Bottenberg, B. Hartigan, A. De Eyto, L. O'Sullivan, E. Rocon, K. Stadler, B. Mazzolai, D. G. Caldwell, J. Ortiz, Pneumatic quasi-passive actuation for soft assistive lower limbs exoskeleton. *Front. Neurorobot.* **14**, 31 (2020).
108. X. Liu, A. Rossi, I. Poulakakis, A switchable parallel elastic actuator and its application to leg design for running robots. *IEEE ASME Trans. Mechatron.* **23**, 2681–2692 (2018).
109. S. Cotton, I. Olaru, M. Bellman, T. van der Ven, J. Godowski, J. Pratt, Fastrunner: A fast, efficient and robust bipedal robot. Concept and planar simulation, in *Proceedings of the 2012 IEEE International Conference on Robotics and Automation (ICRA)* (IEEE, 2012), pp. 2358–2364.
110. S. Cotton, J. Godowski, C. Schmidt-Wetekam, N. Payton, I. M. C. Olaru, J. Pratt, Bipedal running: When leg architecture influences speed, efficiency and robustness, in *Proceedings of the 2012 IEEE International Conference on Robotics and Automation (ICRA)* (IEEE, 2012), pp. 216–217.
111. J. Godowski, U.S. Patent US2013/0192406A1 (2013).
112. S. Seok, A. Wang, M. Y. Chuah, D. J. Hyun, J. Lee, D. M. Otten, J. H. Lang, S. Kim, Design principles for energy-efficient legged locomotion and implementation on the MIT Cheetah robot. *IEEE ASME Trans. Mechatron.* **20**, 1117–1129 (2015).
113. G. Bledt, M. J. Powell, B. Katz, J. Di Carlo, P. M. Wensing, S. Kim, in *Proceedings of the 2018 IEEE/RSJ International Conference on Intelligent Robots and Systems (IROS)* (IEEE, 2018), pp. 2245–2252.
114. F. Roos, H. Johansson, J. Wikander, Optimal selection of motor and gearhead in mechatronic applications. *Mechatronics* **16**, 63–72 (2006).
115. X. Da, R. Hartley, J. W. Grizzle, Supervised learning for stabilizing underactuated bipedal robot locomotion, with outdoor experiments on the wave field, in *Proceedings of the 2017 IEEE International Conference on Robotics and Automation (ICRA)* (IEEE, 2017), pp. 3476–3483.
116. M. van den Broek, thesis, Delft University of Technology (2019).
117. Ö. Drama, A. Spröwitz, Trunk pitch oscillations for energy trade-offs in bipedal running birds and robots. *Bioinspir. Biomim.* **15**, 036013 (2020).
118. S. Cotton, J. C. Godowski, N. R. Payton, M. Vignati, I. Olaru, C. Schmidt-Wetekam, C. Black, U.S. Patent US20160001831A1 (2016).
119. R. Alexander, Optimization and gaits in the locomotion of vertebrates. *Physiol. Rev.* **69**, 1199–1227 (1989).
120. V. A. Tucker, The energetic cost of moving about. *Am. Sci.* **63**, 413–419 (1975).
121. R. L. Marsh, D. J. Ellerby, J. A. Carr, H. T. Henry, C. I. Buchanan, Partitioning the energetics of walking and running: Swinging the limbs is expensive. *Science* **303**, 80–83 (2004).
122. K. A. Rose, R. L. Nudds, J. R. Codd, Intraspecific scaling of the minimum metabolic cost of transport in leghorn chickens (*Gallus gallus domesticus*): Links with limb kinematics, morphometrics and posture. *J. Exp. Biol.* **218**, 1028–1034 (2015).
123. C. P. McGowan, H. A. Duarte, J. B. Main, A. A. Biewener, Effects of load carrying on metabolic cost and hindlimb muscle dynamics in guinea fowl (*Numida meleagris*). *J. Appl. Physiol.* **101**, 1060–1069 (2006).
124. A. J. Ijspeert, A. Crespi, D. Ryczko, J.-M. Cabelguen, From swimming to walking with a salamander robot driven by a spinal cord model. *Science* **315**, 1416–1420 (2007).
125. L. P. Lamas, R. P. Main, J. R. Hutchinson, Ontogenetic scaling patterns and functional anatomy of the pelvic limb musculature in emus (*Dromaius novaehollandiae*). *PeerJ* **2**, e716 (2014).
126. T. J. Roberts, M. S. Chen, C. R. Taylor, Energetics of bipedal running. II. Limb design and running mechanics. *J. Exp. Biol.* **201**, 2753–2762 (1998).
127. M. Ahmadi, M. Buehler, The ARL monopod II running robot: Control and energetics, in *Proceedings of the 1999 IEEE International Conference on Robotics and Automation* (IEEE, 1999), vol. 3, pp. 1689–1694.
128. J. E. Pratt, thesis, Massachusetts Institute of Technology (2000).
129. J. A. Smith, I. Poulakakis, Rotary gallop in the untethered quadrupedal robot scout II, in *Proceedings of the 2004 IEEE/RSJ International Conference on Intelligent Robots and Systems, 2004. (IROS 2004)* (IEEE, 2004), vol. 3, pp. 2556–2561.
130. M. Hutter, C. Gehring, M. A. Höpflinger, M. Blosch, R. Siegwart, Toward combining speed, efficiency, versatility, and robustness in an autonomous quadruped. *IEEE Trans. Robot.* **30**, 1427–1440 (2014).
131. H.-W. Park, S. Park, S. Kim, Variable-speed quadrupedal bounding using impulse planning: Untethered high-speed 3D Running of MIT Cheetah 2, in *Proceedings of the 2015 IEEE International Conference on Robotics and Automation (ICRA)* (IEEE, 2015), pp. 5163–5170.
132. S. Kitano, S. Hirose, A. Horigome, G. Endo, TITAN-XIII: Sprawling-type quadruped robot with ability of fast and energy-efficient walking. *Robomech J.* **3**, 8 (2016).
133. X. Liu, A. Rossi, I. Poulakakis, SPEAR: A monopedal robot with switchable parallel elastic actuation, in *Proceedings of the 2015 IEEE/RSJ International Conference on Intelligent Robots and Systems (IROS)* (IEEE, 2015), pp. 5142–5147.

Acknowledgments: A.A.S. thanks the International Max Planck Research School for Intelligent Systems (IMPRS-IS) for support. We would like to thank E. Badri for discussions and support developing the coupling mechanism concept and processing data, L.P. Lamas and J.R. Hutchinson for providing access to the emu cadaver, and the members of the MPI-IS mechanical workshop for manufacturing the large BirdBot model leg. **Funding:** This work was funded by the Max Planck Society, and by a Human Frontier Science Program grant (RGY0062/2010) to M.A.D. **Author contributions:** M.A.D. contributed to conceptualization and planning, materials, and resources for biology experiments. A.B.-S. conceived and planned the research, developed the nonmotorized prototype, performed cadaver experiments, and analyzed data. A.A.S. designed and implemented the robot and the experimental setup, performed the robot experiments, and analyzed the robot data. M.S. contributed to research planning, materials and resources, and editing. M.A.D., A.B.-S., and M.S. supervised the research. M.A.D. and A.B.-S. wrote the manuscript with assistance from A.A.S. and M.S. All authors contributed to the interpretation and discussion of the data. **Competing interests:** A European and international patent (no. EP 19157793.1) related to this work has been submitted. The authors declare that they have no other competing interests. **Data and materials availability:** All data needed to evaluate the conclusions of the paper are available in the paper or the Supplementary Materials. Additional data and the BirdBot's computer-aided design model are available as MPDL Edmond dataset.

Submitted 11 January 2021
Accepted 22 February 2022
Published 16 March 2022
10.1126/scirobotics.abg4055

Science Robotics

BirdBot achieves energy-efficient gait with minimal control using avian-inspired leg clutching

Alexander Badri-SpröwitzAlborz Aghamaleki SarvestaniMetin SittiMonica A. Daley

Sci. Robot., 7 (64), eabg4055. • DOI: 10.1126/scirobotics.abg4055

Science Robotics (ISSN) is published by the American Association for the Advancement of Science. 1200 New York Avenue NW, Washington, DC 20005. The title *Science Robotics* is a registered trademark of AAAS.